

2009

Catalytic carbon nanotube growth by through thin film ablation and infrared laser heating

Brandon M. Black
University of Dayton

Follow this and additional works at: https://ecommons.udayton.edu/graduate_theses

Recommended Citation

Black, Brandon M., "Catalytic carbon nanotube growth by through thin film ablation and infrared laser heating" (2009). *Graduate Theses and Dissertations*. 1572.
https://ecommons.udayton.edu/graduate_theses/1572

This Thesis is brought to you for free and open access by the Theses and Dissertations at eCommons. It has been accepted for inclusion in Graduate Theses and Dissertations by an authorized administrator of eCommons. For more information, please contact mschlangen1@udayton.edu, ecommons@udayton.edu.

**CATALYTIC CARBON NANOTUBE GROWTH BY THROUGH THIN
FILM ABLATION AND INFRARED LASER HEATING**

Thesis

Submitted to

The School of Engineering of the
UNIVERSITY OF DAYTON

In Partial Fulfillment of the Requirements for

The Degree

Master of Science in Materials Engineering

By

Brandon M. Black

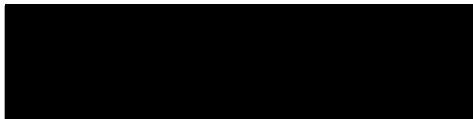
UNIVERSITY OF DAYTON

Dayton, OH

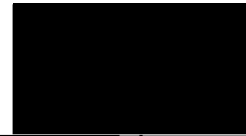
May 2009

CATALYTIC CARBON NANOTUBE GROWTH BY THROUGH THIN FILM
ABLATION AND INFRARED LASER HEATING

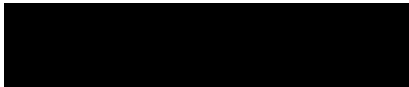
APPROVED BY:



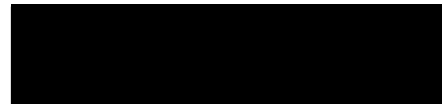
P. Terrence Murray, Ph.D.
Committee Chairman
Professor
Graduate Materials Engineering
Program



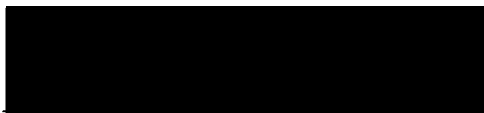
Liming Dai, Ph.D.
Advisory Committee Member
Professor
Graduate Materials Engineering
Program



Pani Varanisi, Ph.D.
Advisory Committee Member
Materials Research Engineer
University of Dayton Research
Institute



Benji Maruyama, Ph.D.
Advisory Committee Member
Materials Research Engineer
Air Force Research Laboratory



Malcolm W. Daniels, Ph.D.
Associate Dean
School of Engineering



Joseph E. Saliba, Ph.D., P.E.
Dean, School of Engineering

ABSTRACT

CATALYTIC CARBON NANOTUBE GROWTH BY THROUGH THIN FILM ABLATION AND INFRARED LASER HEATING

Name: Black, Brandon Matthew

University of Dayton, 2009

Advisory Committee Chairman: Dr. Paul 'Terry' Murray

A technique for carbon nanotube growth was developed based upon Through Thin Film Ablation (TTFA). TTFA was used to generate floating metal catalysts in a low pressure ethylene/argon atmosphere heated by a 10.6 μm CO₂ laser. Steady state pressure was maintained with a mechanical vacuum pump while controlled argon mass flow provided a background for nanoparticle formation and carried products through the reaction chamber. Ethylene was used under controlled mass flow as a carbon feedstock for nanotube growth.

Nine experiments were conducted to gain an understanding of the variables; pressure, hydrocarbon/background gas ratio and heating laser power. Samples were characterized with Raman spectroscopy, Scanning Electron Microscopy (SEM), and Transmission Electron Microscopy (TEM).

The results of this work indicate that both ethylene (g) and carbon (s) were heated rapidly when illuminated by the Infrared CO₂ laser. The outcome is a two step growth process; First catalytic growth of CNTs occurs, then a pyrolytic deposition of amorphous carbon follows. Further optimization of hydrocarbon/background gas ratio is necessary

to eliminate unwanted products; even so TTFA in concert with IR laser heating is shown as viable way to grow CNTs.

ACKNOWLEDGMENTS

Many thanks to AFRL/RZPG for funding this effort:

Specific thanks to Dr. Paul Barnes, Capt. John Bulmer Mr. Kevin Yost and Dr. Chakrapani 'Pani' Varanasi for providing me with the opportunity to undertake this challenging research topic.

The author would like to acknowledge:

My wife, Crystal, for her love, support and understanding.

Dr. Terry Murray for his confidence in my abilities, technical guidance and motivation.

Dr. Benji Mayruama for sharing his expertise in nanotechnology, particularly in the area of carbon nanotube nucleation and growth.

Dr. Eunsung Shin for all the help, training and advice provided. He offered invaluable assistance by depositing thin films and aligning the optics.

Mr. Neal Pierce for insights into previous TTFA research and development.

Dr. Larry Dosser for his expertise and technical discussions.

My Colleagues from AFRL/RXB:

Mr. Kevin Davis for his help with Microscopy, CAD design and meaningful discussions on carbon nanotube synthesis.

Mr. Max Alexander for insight into the physics of CNT conductivity.

Mrs. Heather Dowty for assistance with proofreading and revising.

TABLE OF CONTENTS

ABSTRACT.....	- iii -
ACKNOWLEDGEMENTS	-v-
LIST OF FIGURES.....	-viii -
 CHAPTER 1: INTRODUCTION AND BACKGROUND.....	- 1 -
1.1 Thesis Introduction.....	- 1 -
1.2 Carbon Nanotubes and Their Properties	- 3 -
1.3 Potential Applications.....	- 9 -
1.4 CNT Synthesis Methods	- 13 -
1.4.1 Arc Discharge, CVD and HiPCO	- 13 -
1.4.2 PLA and the Laser Oven Method for SWNT Growth	- 15 -
1.4.3 Through Thin Film Ablation	- 16 -
1.5 Fabrication of Small Diameter Single-Wall Carbon Nanotubes	- 19 -
1.6 Rationale for this Work.....	- 20 -
 CHAPTER 2: EXPERIMENTAL PROCEDURES	- 23 -
2.1 Design and Assembly of Apparatus.....	- 23 -
2.2 Experimental Procedure	- 34 -
2.3 Description of Experiments.....	- 39 -

2.4 Characterization - Raman Spectroscopy	- 50 -
CHAPTER 3: RESULTS AND DISCUSSION	- 51 -
3.1 Results	- 51 -
3.2 Discussion.....	- 80 -
CHAPTER 4: SUMMARY AND FUTURE WORK.....	- 83 -
4.1 Summary.....	- 83 -
4.2 Future Work.....	- 83 -
Appendix.....	- 84 -
References.....	-86-

LIST OF FIGURES

Figure 1 Molecular diagram of a SWNT next to a MWNT.....	- 4 -
Figure 2 TEM micrograph of a MWNT	- 6 -
Figure 3 Plot of Conductance vs. Distance for a MWNT.....	- 7 -
Figure 4 Illustration and TEM micrograph showing VGCNF stacked graphitic sheets.....	- 8 -
Figure 5 Diagram of CNT root growth in comparison to tip growth.....	- 14 -
Figure 6 A) Pulsed Laser Ablation (PLA) and B) Through Thin Film Ablation (TTFA).....	- 18 -
Figure 7 Catalyst particles illuminated by the ablation laser	- 22 -
Figure 8 Cutting of aluminum stock for optical bench stand.....	- 24 -
Figure 9 Optical bench stand assembly	- 25 -
Figure 10 Mounting stand to optical bench	- 26 -
Figure 11 Assembly of the reaction chamber	- 27 -
Figure 12 Reaction chamber nearing completion	- 28 -
Figure 13 Completed reaction chamber on optical bench stand	- 29 -
Figure 14 Layout of the experimental apparatus	- 30 -
Figure 15 Diagram of CAD designed rotator extension	- 32 -
Figure 16 Fused silica disk with nickel thin film mounted.....	- 33 -
Figure 17 Nickel thin film deposition in progress	- 35 -
Figure 18 Sample collection points.....	- 37 -
Figure 19 Pressure vs. argon mass flow rate.....	- 40 -
Figure 20 Pressure vs. ethylene mass flow rate	- 41 -

Figure 21 Pressure vs. ethylene mass flow rate	- 42 -
Figure 22 Nickel thin film before and after ablation	- 44 -
Figure 23 Ablation plume from experiment #0	- 45 -
Figure 24 Photo micrograph and Raman spectrum from experiment #1	- 52 -
Figure 25 TEM micrograph of a 38 nm carbon shell from experiment #0.....	- 53 -
Figure 26 TEM micrograph of a 41 nm carbon shell from experiment #0.....	- 54 -
Figure 27 Raman spectrum from experiment #4	- 56 -
Figure 28 Photomicrograph of carbon specimen obtained from experiment #4	- 57 -
Figure 29 TEM micrograph from experiment #4 showing a large carbon island.....	- 58 -
Figure 30 TEM micrograph from experiment #4 showing large carbon masses.....	- 59 -
Figure 31 TEM micrograph from experiment #4 showing a 73 nm tube-like feature..	- 60 -
Figure 32 TEM micrograph from experiment #4 showing a 48 nm tube-like feature..	- 61 -
Figure 33 TEM micrograph from experiment #4 showing a 17 nm diameter CNT	- 62 -
Figure 34 TEM micrograph from experiment #4 showing a 21 nm CNT protruding from a carbon mass	- 63 -
Figure 35 Raman spectrum obtained from experiment #5.....	- 65 -
Figure 36 Photomicrograph of the material measured from experiment #5	- 66 -
Figure 37 Photomicrograph of the material measured from experiment #6	- 67 -
Figure 38 Raman spectrum obtained from experiment #6.....	- 68 -
Figure 39 SEM micrograph of nanoparticles from experiment #5	- 70 -
Figure 40 SEM micrograph of nanoparticles from experiment #6	- 71 -
Figure 41 TEM micrograph from experiment #7 showing a 1.2 nm diameter CNT	- 73 -
Figure 42 TEM micrograph from experiment #7 showing a 3.7 nm diameter CNT	- 74 -

Figure 43 TEM micrograph from experiment #7 showing a 2.6 nm diameter MWCNT	- 75 -
Figure 44 TEM micrograph of a CNT protruding from a larger carbon mass	- 77 -
Figure 45 An intentionally over-focused TEM micrograph showing many tube-like features	- 78 -
Figure 46 TEM micrograph of interesting wall-like features	- 79 -
Figure 47 Infrared spectrum of ethylene at 600 Torr with path length of 5 cm from the NIST webbook	- 81 -
Figure 48 Close up of 9.0 – 11.5 μm region of ethylene IR spectrum from the NIST	- 82 -
Figure 49 Illustration of three different SWNT chiralities	- 84 -
Figure 50 Diagram from H. Dai showing different SWNT structures with description of corresponding electronic properties.....	- 85 -

Chapter 1

Introduction and Background

1.1 Thesis Introduction

It may be disputed as to when the carbon nanotube (CNT) was actually discovered, but interest in nanoscale carbon filaments greatly accelerated when Kroto and Smalley reported C_{60} fullerenes in 1985 [1]. Seven years later, while studying carbon fullerenes formed by the arc discharge method [2,3], S. Iijima reported the Multi-Wall Carbon Nanotube (MWNT) [4]. The Single-Wall Carbon Nanotube (SWNT) was reported in 1993 by the same group studying metal filled carbon nanocapsules [5]. This was particularly important because nanoscale carbon filaments and fibers had been studied for many years, but the concept of a rolled single graphene sheet was previously thought impossible [6].

The pi-bonded structure of CNT, both single and multi-wall had incredibly high aspect ratios which were very intriguing to the material science community. The structure had implications of high thermal and electrical conductivity as well as extremely high tensile strength in the same morphology. The extraordinary intrinsic properties and great number of potential applications created an explosion in nanotechnology research and development [7].

Yet with more than fifteen years of extensive research and development, no one has been able to produce sizable quantities of Single-Walled Carbon Nanotubes (SWNTs) with controlled electrical and mechanical properties [8]. This is because the

properties of a nanotube are dependent upon chirality, which is exceedingly difficult to control. Chirality depends upon the diameter of the nanotube and the arrangement of carbon atoms within. There are many chiral groups, a proportion of which are semiconducting with a smaller quantity that possess metallic conductive properties. Metallic CNTs are the most desirable for electronic applications, but make up only one-third of the product synthesized [9]. Semiconducting nanotubes and carbon soot make up the remainder.

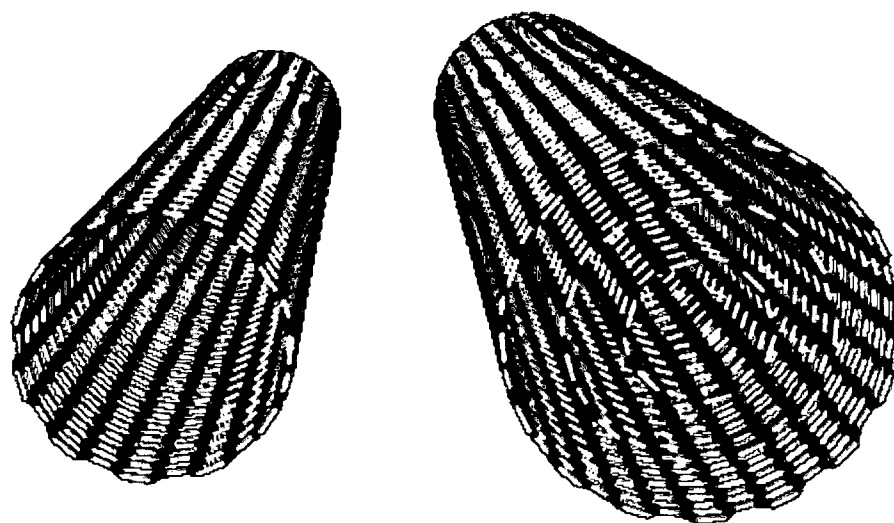
Many methods for synthesizing carbon nanotubes have been developed with various yields and degrees of quality, but none have achieved industrial scale production with high quality. Because of this, the cost of purified SWNTs remains high. Currently, one pound with purity of 90% is \$12,000 [10]. As a result SWNT use has been restricted to exotic applications where weight reduction is of utmost importance and cost is a secondary consideration. Clearly, much work remains before high quality CNTs can be affordably utilized in everyday applications.

The purpose of this work is to explore Through Thin-Film Laser Ablation (TTFA) as a method for generating floating carbon nanotube catalysts. The narrow distribution of small catalyst particles generated by TTFA should produce more small diameter SWNTs. Because metallic SWNTs typically have small diameters, TTFA may produce a higher yield of metallic CNTs. An additional motivation for using this method is the potential to grow longer carbon nanotubes. Floating catalysts are unconstrained allowing nanotubes to grow freely without interference. If nanotubes could reliably be grown to longer lengths, they could be used to replace metallic conductors such as copper.

The goals of this thesis are as follows: 1) provide the reader with a basic understanding of CNT types, properties and applications, 2) explain our work and the rationale supporting it, 3) discuss the results of our work and how they contribute to the field of CNT research.

1.2 Carbon Nanotubes and Their Properties

There are multiple types of carbon nanotubes (CNTs), but the simplest structure is of a Single-Wall Carbon Nanotube (SWNT). It can be described as a sheet of graphene rolled into a continuous, small cylinder with a hemispherical cap at one or both ends [11]. Because SWNTs and graphene are so similar their physical properties are comparable. The diameter of a SWNT ranges from 0.4 nm [12] up to a few nanometers. A sketch of a SWNT next to a MWNT can be found in Figure 1. Physically, SWNTs have a high degree of perfection in their hexagonal sp^2 hybridized carbon bonds [13]. Molecular mechanic based finite element modeling by M. Meo et al. reported the average Young's modulus for several types of SWNTs near 1 TPa [14] giving them five times the modulus of steel [13]. Perhaps the most impressive property of SWNTs is extremely high electrical conductivity. Early measurements of metallic SWNTs by the direct four-point technique were less than $10^{-4} \Omega\text{-cm}$ as reported by Thess *et al.* [15]. Z. Yao et. al. measured the current carrying capacity of SWNTs at 10^9 A/cm^2 [16] while in a later study, P. Avouris [17] reported that stable current densities could be pushed as high as 10^{13} A/cm^2 . In comparison, copper thermally decomposes at current densities above $3 \times 10^7 \text{ A/cm}^2$ due to extreme Joule heating [18].



SWNT

MWNT

Figure 1 Molecular diagram of a SWNT next to a MWNT [19]

Another type of CNT, the Multi-Wall Carbon Nanotube (MWNT) can be visualized as multiple individual, concentric nanotubes with increasing diameter [20]. When viewed end on, the walls of a MWNT look like the rings of a tree as the insert in Figure 2 shows. A MWNT with two walls can be as small as 0.5 nm in diameter [21]. As the number of walls increases, so does the diameter. Diameters can be up to tens of nanometers. A TEM micrograph of a MWNT is given in Figure 2.

MWNTs like SWNTs have interesting electrical properties. The resistance of a given MWNT depends upon the location of metallic tubes within. If a metallic tube is found on the surface, then its electronic properties will dominate [22]. If a metallic tube is located underneath semi-conducting tubes, resistance increases stepwise into the MWNT structure until electrons reach a highly conductive tube. This leads to a wide variance of conductivity in MWNTs [23]. A plot of conductance vs. position from Frank *et al.* is located in Figure 3 depicting this. MWNTs also have impressive mechanical strength. The Young's modulus of a given MWNT however varies highly with the degree of disorder in the graphitic structure of the MWNT [24]. Higher disorder leads to lower mechanical as well as lower electronic properties.

While not technically a carbon nanotube, the Vapor Grown Carbon Nanofiber (VGCNF) possesses some of the properties of CNTs and can be made in large quantities [20]. VGCNFs are much larger in diameter, ranging from 60 nm up to 200 nm [25]. Rather than rolled graphitic sheets, they are comprised of stacked graphitic planes as pictured in Figure 4. Because this structure is not axially continuous and contains more disorder, the physical and electrical properties are significantly lower than CNTs. Their properties, however, are still appealing for many applications due to their low cost [20].

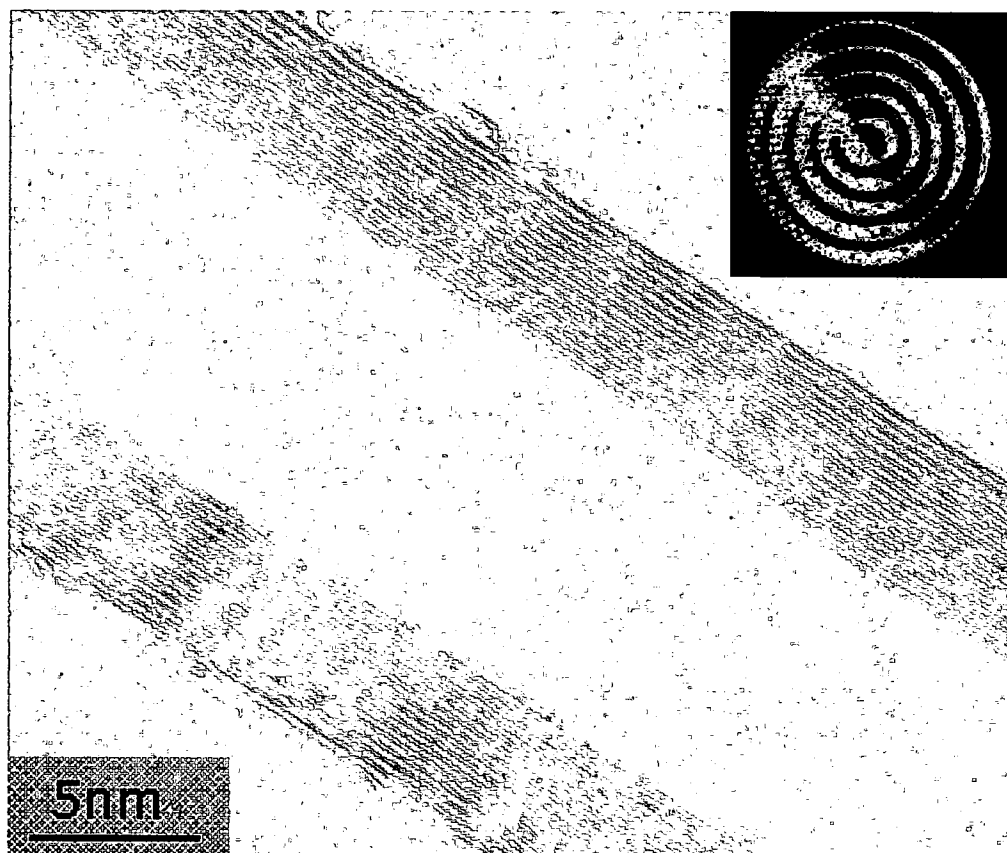


Figure 2 TEM micrograph of a MWNT [26]

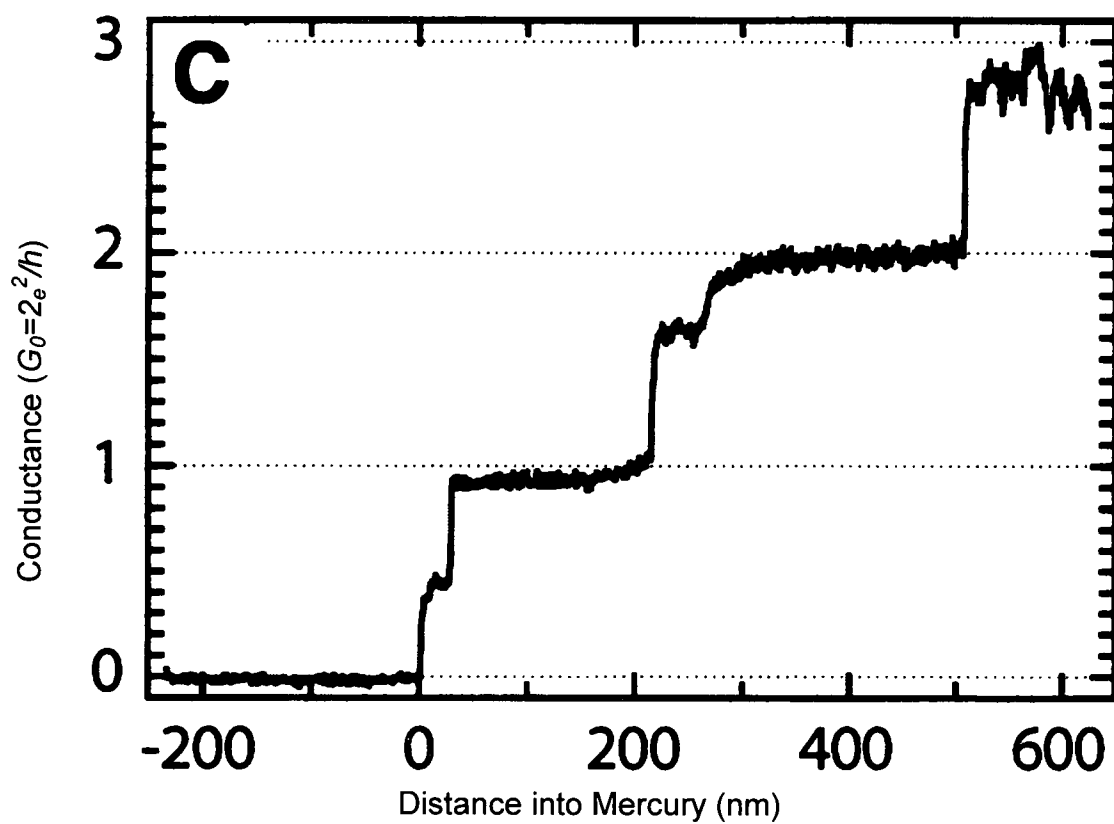


Figure 3 Plot of Conductance vs. Distance for a MWNT [27]

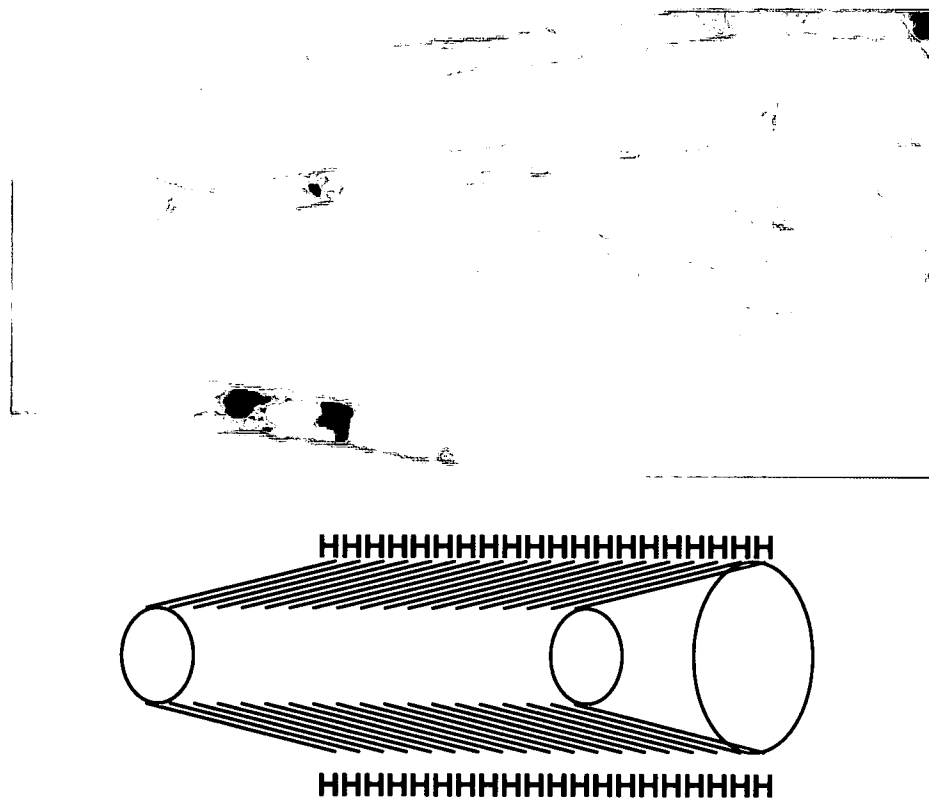


Figure 4 Illustration and TEM micrograph showing VGCNF stacked graphitic sheets [20]

1.3 Potential Applications

A myriad of applications have been proposed for CNTs based upon their unique attributes. The geometry of SWNTs is an excellent candidate for hydrogen storage. The hollow core is capable of drawing condensing gasses through capillary action [28]. The mechanical properties of CNTs are excellent for replacing typical carbon, glass, and Kevlar fibers in lightweight structural composites [29,30,31]. The high thermal conduction of CNTs suggests that they are excellent nanoscale heat pipes [32]. The electronic applications for CNTs are numerous as well. Because a CNT can be both a semiconductor and a conductor, there is much work towards developing nanotransistors [33]. There is hope that one day they will be the key element of nanoelectronic devices [34]. They are excellent electrode materials for batteries and capacitors because they have extremely high surface area and low resistivity [35]. They also make excellent field emitters for flat-panel displays. It is rumored that CNTs will be utilized in commercial flat-panel televisions within the next few years [36].

The extremely high current carrying capacity of CNT's makes them an excellent candidate for replacing metal conductors. One application that has received much attention is for Electromagnetic Interference (EMI) shielding materials [37]. Typically metal sheets or foils of aluminum are constructed to create a Faraday cage that attenuates unwanted external electromagnetic waves [38]. These waves can cause interference which degrades the performance of devices such as communication radios, wireless phones and computers. Metal sheets are effective but can be heavy and difficult to retrofit in existing applications. Foils save weight but require conductive adhesives to form a good seal and can be damaged easily.

CNTs can be dispersed into non-conductive host matrices such as thermoplastic polymers and thermoset resins to create conductive networks. This can be accomplished easily due to CNTs long length and small diameter, or 'high-aspect ratio' [39]. Electrical percolation can be achieved at loadings as low as 0.1% by weight [40], giving a significant weight savings over metallic shielding materials. The level of Shielding Effectiveness (SE) required for a specific application can be tailored by controlling the CNT loading. Beyond a significant weight savings polymer nanocomposites can easily be extruded, molded or spray applied making them ideal for incorporation into manufacturing processes or in retrofit applications [41].

Another application that takes advantage of the high electrical conductivity of metallic CNTs is replacing copper wires. Silver is the most conductive metal in the periodic table. But due to the high cost and a density of 10.49 g/cm^3 [42] it is only used in applications that require extremely high fidelity. Copper is an excellent conductor, second only to silver, and has a slightly lower density of 8.94 g/cm^3 [42]. The density of a CNT varies depending upon the chirality, but ranges between 1.2 and 2.0 g/cm^3 [43]. This means that a SWNT wire could be made at least 85% lighter than a given copper wire.

This makes CNT conductors very appealing for large aircraft where large amounts of wiring needed to communicate with the many systems on board. As an example a Boeing 747-400 contains more than 135 miles of copper wire which weighs 2 tons [44]. Hundreds of pounds of weight savings could be realized which would increase the effective range of the aircraft or allow heavier payloads to be carried. A CNT wire would also be excellent for applications where a cable is required to flex or bend flex

repeatedly. Fatigue life becomes a concern when using metal for such purposes, but CNT's are capable of sustaining large elastic deformations without damage [45]. They would be capable of performing in a harsh environment for millions of cycles.

Additionally, CNT wires have potential for being multifunctional [46,47], something previously thought impossible with copper or aluminum conductors. The extremely high strength of a CNT wire could be used as a mechanical reinforcement in the structure of an aircraft. This would further reduce weight by removing traditional wires and replacing structural materials in the airframe.

The shortcoming of CNTs produced today is their length. Conventional copper wires are not made of short conductive elements; they are made of continuous strands. This is because the contact resistance between the filaments is additive. In the same way, a wire made with nanotubes would have non-trivial resistance due to a high number of contact sites. The sum of resistances between CNTs would mitigate the high conductivity of the individual nanotubes until CNTs were made longer than a critical length. The caveat here is the difficult task of controlling chirality and thus keeping high conductivity.

This is where an understanding of the conduction mechanism of a CNT becomes important. Metals such as silver, copper or aluminum rely on free electrons in valence shells. In bulk copper, for example, nearly every valence shell electron contributes to conduction. This gives copper high charge transport in all three axes. CNT's, however, conduct under a different mechanism. Electrical conductivity in CNTs is a result of delocalization of π bonds from unhybridized p orbitals [48]. The electron carrying potential of a nanotube is based upon chirality. The angle at which the 'rolled graphitic

sheet' is formed gives the locations of the carbon atoms and determines the chiral nature.

While a lengthy discussion of chirality is not appropriate here, selected excerpts are located in the Appendix in order to give the reader a better understanding.

1.4 CNT Synthesis Methods

1.4.1 Arc Discharge, CVD and HiPCO

There are many methods for synthesizing CNTs. The arc discharge method was developed to study carbon fullerenes, but was responsible for the first reporting of the CNT [4]. Arc Discharge involves placing two graphite rods in close proximity to one another in an enclosed helium atmosphere. A current of approximately 100 A is passed through the graphite rods, which heats them to over 2500°C vaporizing the carbon [49]. As the carbon cools it condenses throughout the reaction vessel. When pure graphite rods are used MWNTs can be found on the negatively biased graphite rod along with carbon fullerenes and soot. For SWNT growth, the anodic graphite rod can be doped with a low percentage, approximately 1-4 at.%, metal catalyst particles. Typically Fe, Ni, or Co is used. This method produces a low yield of CNTs amidst the carbon byproducts and is a batch process.

Chemical Vapor Deposition (CVD) [50] involves heating a reactor to sufficient temperature to thermally decompose a hydrocarbon gas with catalyst present. The catalyst particles can be patterned onto a substrate or floating in the reaction chamber. When fixed to a substrate, the catalyst can facilitate CNT growth in two different ways. The first is called 'root growth' where the catalyst remains attached to the substrate and the CNT grows upwards. The second method is called 'tip growth' where the catalyst lifts off of the substrate and the nanotube grows underneath the catalyst [51]. A diagram showing the differences in base growth and tip growth is located in Figure 5. Temperatures typically range from 650°C to 1100°C while methane and ethylene are

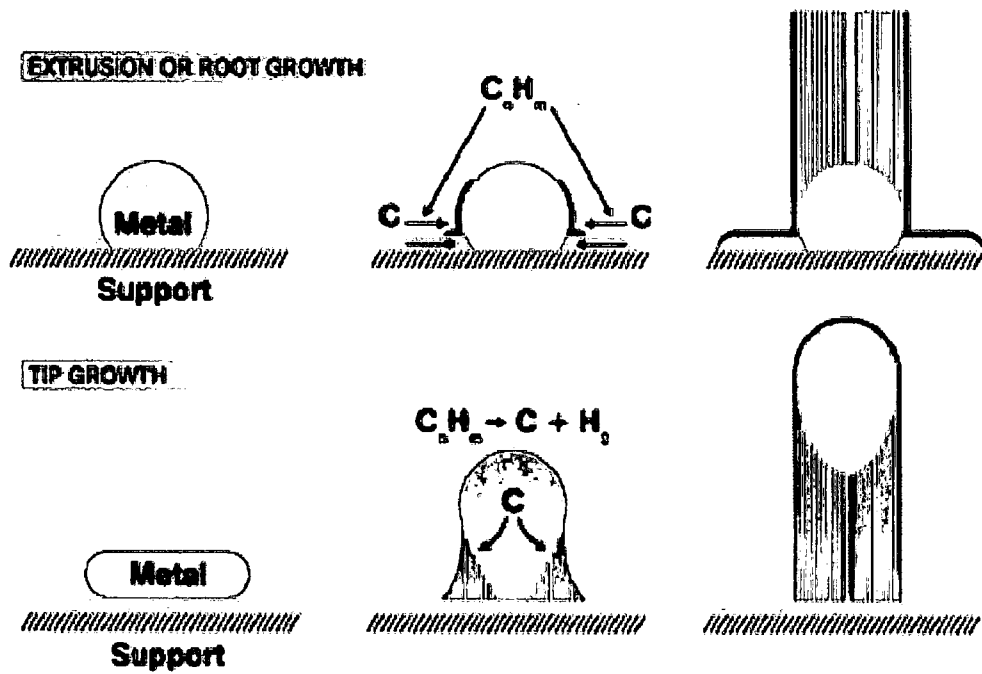


Figure 5 Diagram of CNT root growth in comparison to tip growth [51]

commonly used as carbon feedstock [52]. CVD can also be enhanced with plasma in order to align and accelerate CNT growth.

The High Pressure Carbon monoxide (HiPCO) synthesis method developed by Smalley *et al.* in 1999 is a form of CVD that does not use a substrate. Rather iron pentacarbonyl, $\text{Fe}(\text{CO})_5$ (l) is used as an iron containing catalyst precursor. Pressurized CO is injected with the $\text{Fe}(\text{CO})_5$ precursor in an oven at a temperature between 800°C and 1200°C. The flow of gases in the oven carries the products through the chamber. The advantage of this process is that CO is the carbon feedstock, which limits the amount of excess carbon deposited on CNTs [53]. The primary byproduct of the reaction is CO_2 which is easily removed. This reaction can be run continuously but yields only range between 25 – 45 % by weight.

1.4.2 PLA and the Laser Oven Method for SWNT Growth

Pulsed Laser Ablation (PLA) is a process where a high energy laser is focused onto a metal or organic material. While the absorption or reflection characteristics of a material affect how a material interacts at a given wavelength, the energy density at the focal point is high enough in PLA to vaporize the material. Each pulse contains a large number of photons arriving at the same point in a short period of time. The technique is used to generate thin films when performed in a vacuum [54] or to generate nanoparticles in a low pressure background gas [54]. Materials generated by PLA are inherently high in purity because there are no chemical precursors necessary; the materials ablated are the materials received [54].

The laser oven method [55] for growing SWNTs has been known as a simple method for producing high quality ropes in small quantities [56]. In this method, a

pulsed laser is focused on a solid carbon pellet or rod doped with metal catalyst. The ablated material from each laser pulse is ejected into a heated oven that ranges between 900°C and 1200°C. The advantage of this method is that parameters such as temperature, pressure and laser power can be controlled very precisely [57]. SWNT yields are typically high with PLA, which are normally greater than 70% [56]. Unfortunately, the laser oven method is a batch process and scale-up has proven to be challenging.

1.4.3 Through Thin Film Ablation

Pulsed laser ablation as a technique for generating nanoparticles has drawbacks. The primary problem is that nanoparticles ablated are frequently agglomerated [54]. Secondly, the distribution of particles is bimodal with both nano-sized particles and μm -sized products. It is believed that large μm -sized particles are a result of ‘splashing’ [58,59]. Splashing has been attributed to the temperature gradient formed in the thickness of the irradiated material. Material on the surface receives sufficient energy to be vaporized while matter within is progressively heated to a lesser degree. Below the vaporized layer, a region of liquid droplets is formed where T_m has been reached resulting in subsurface boiling and exfoliation [59]. A portion of these “laser droplets” receive sufficient energy from recoil forces to be ejected with the atomic species [59]. Large particles and agglomeration are both detrimental to nanotube growth. The large particles and smaller particles bundled together reduce the available surface area for available for catalytic activity. It is also believed that agglomerated catalyst may produce entangled CNTs [60]. Once CNTs are agglomerated they are extremely difficult to detangle and disperse.

The Through Thin Film laser Ablation (TTFA) method developed by Murray, *et al.* differs from conventional PLA by ablating the material *through* a UV transparent support rather than directly from the material surface. Diagrams depicting PLA and TTFA are located in Figure 6. TTFA produces a narrow size distribution of nanoparticles that are generally free from agglomeration due to the elimination of splashing [61]. Another advantage is that the laser does not propagate through the plume of ablated material thereby eliminating uncontrolled secondary interactions.

In TTFA the ablated material is ejected in a tight plume normal to the surface of the fused silica support. The laser pulse yields two product forms, ablated material and vaporized material. The rate of atomic recombination of the vaporized material is governed by the type and pressure of the background gas. With more atoms present (higher background gas pressure) the number of collisions the atomic species has with the background gas is increased. These collisions transfer energy to the gas and the energy of the metal atoms is reduced. This energy reduction, both thermal and kinetic, rapidly cools the atoms forming a narrow size distribution of particles centered around 2 nm.

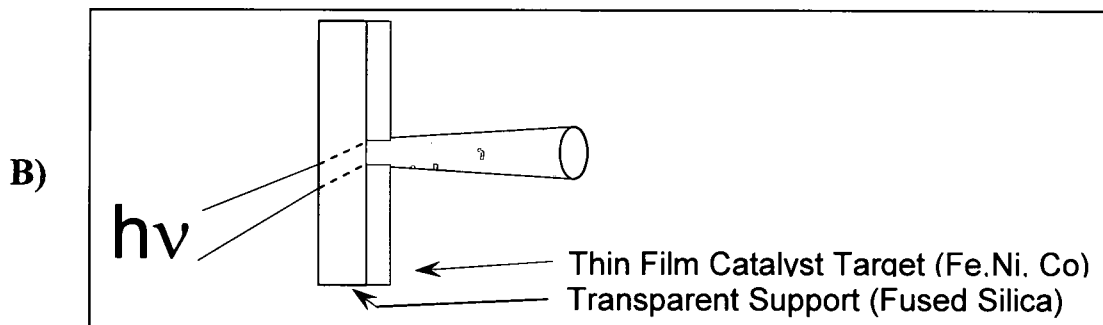
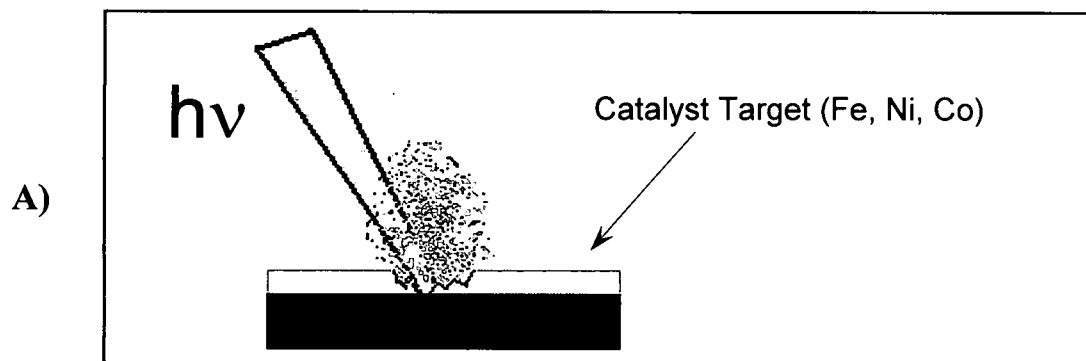


Figure 6 A) Pulsed Laser Ablation (PLA) and B) Through Thin Film Ablation (TTFA)

1.5 Fabrication of Small Diameter Single-Wall Carbon Nanotubes

The advantage of the TTFA method may be due to the critical role that the size of the catalyst plays in growth of carbon nanotubes. Many argue that CNTs grow readily once a stable carbon cap or hemisphere is formed. The formation of the cap is said to be primarily dependent upon the diameter of the catalyst nanoparticle [62]. S. Huang has even shown that materials inactive as carbon catalysts are capable of growing nanotubes as long as they are of the proper size [63]. Previous work in Dr. Murray's group has shown that these theories are plausible. The small agglomeration-free nanoparticles produced with TTFA created long SWNTs that were not entangled [59]. Unfortunately, two chambers were needed for this work. One chamber was used to ablate a metal catalyst by TTFA and a separate CVD chamber was used to grow CNTs from the nanoparticles.

In an attempt to simplify the process and grow CNTs in a single chamber, hydrocarbon gas was injected with the background gas during TTFA. This work generated products that appear to have gone through the very beginnings of CNT growth. These 'fetal' carbon/catalyst particles were discovered amongst spherical carbon coated catalyst nanoparticles. The presence of these CNT 'fetuses' implied that growth time was much too short for growth to occur. Indeed, high speed imagery of the ablated plume of material showed that catalyst particles were at growth temperatures for less than 500 μ s.

1.6 Rationale for this Work

The goal of growing SWNTs with the TTFA method in one step was still very appealing. The answer to the challenge of increasing the growth time seemed relatively straightforward; it was apparent that a heat source, in addition to the thermal component from ablation, was necessary. Two options were considered for providing additional heat, a tube furnace and a CO₂ laser. The CO₂ laser was chosen because heat could be introduced directly at the end of the plasma hot zone rather than downstream after the particles had cooled.

The question of whether or not nanoparticles could be motivated to travel along the path of the heating laser was answered by imagery from previous work located in Figure 7. This frame shows the ablation laser entering the chamber which was significant because the KrF Excimer is invisible to the human eye at $\lambda=248$ nm. In this instance, however, nanoparticles from the previous laser pulse had floated around behind the target and were fluorescing from incident laser energy. This ease at which the nanoparticles were suspended in a static chamber suggested that they could be readily moved through the chamber with flowing gas.

The questions that remained, however, were many. The main unknown was to what degree the floating particles would interact with the CO₂ laser. Carbon (s) and many hydrocarbon gasses are absorptive of Infrared (IR) energy to a high degree. The expectation was that carbon hemispheres would form on the catalyst nanoparticles from ablation. These particles would then be heated rapidly by the CO₂ laser and CNTs would grow. As the CNTs grew they would continue to absorb IR energy and be heated in the same manner. This assumption, however, depended upon the floating particles reaching

sufficient growth temperatures. Calculation of particle temperature flowing through the system was far too complex for the scope of this work, so assembly of a suitable chamber was taken underway.

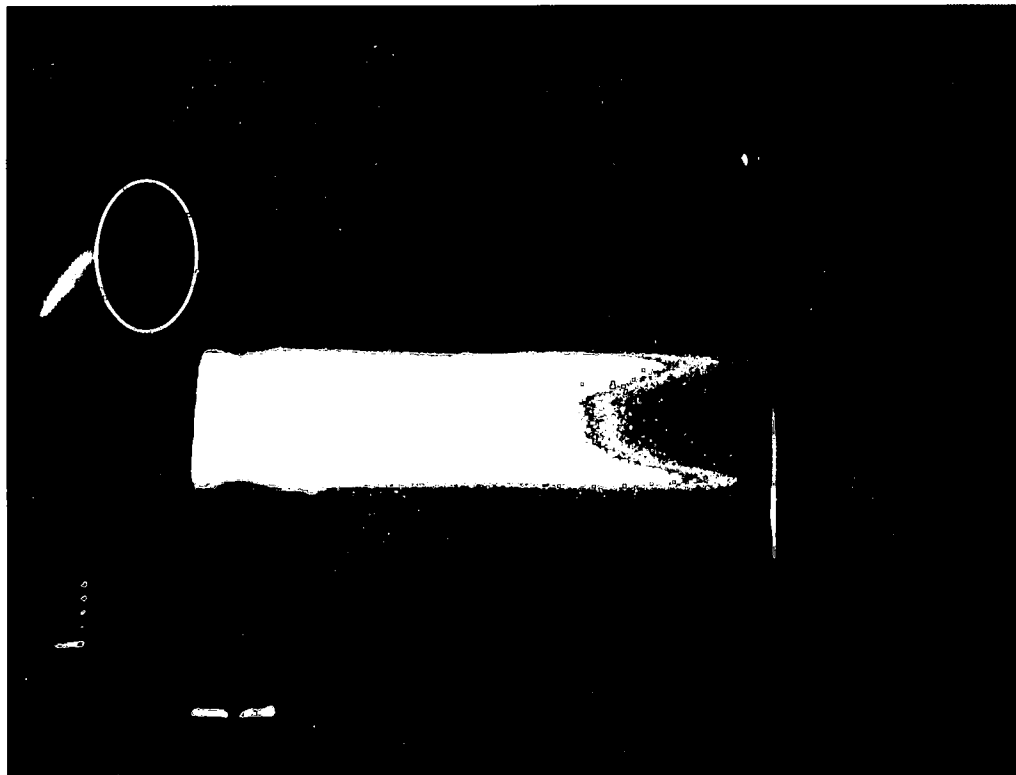


Figure 7 Catalyst particles (circled) illuminated by the ablation laser

Chapter 2

Experimental Procedures

2.1 Design and Assembly of Apparatus

The reaction chamber and optical bench stand were designed and fabricated with guidance from Dr. Terry Murray and Dr. Eunsung Shin. The foundation for the system was a 304 Stainless Steel vacuum chamber having eight ports around the circumference and a large window for sample access on top. Four ports perpendicular to one another were used for laser propagation. One pair of ports was utilized for the ablation laser with UV transparent windows and a beam kill. The other two ports were equipped with Ceramtec 19163-02-CF IR transparent windows for the heating laser. A series of pictures depicting the progress from optical bench stand to completed chamber are located in Figures 8, 9, 10, 11, 12 and 13. Additionally, a diagram depicting the layout of the entire system and the laser positions on the optical bench is located in Figure 14.

The ablation laser, a Spectra Physics krypton-fluoride excimer ($\lambda = 248 \text{ nm}$), is capable of 125W maximum average power with pulse power up to 1 Joule. The ablation laser beam is reduced to 10 mm in diameter with an aperture before reflecting off of a series of mirrors directing it towards the chamber. Just before entering the chamber a biconvex lens with focal length of 172 mm is used to focus the beam into an ovate area of 6.5 mm x 3.5 mm on the thin film target. The power density at the target is 560 mJ/cm^2 per pulse. The laser beam impinges upon the thin film at an angle of 45° , but ejects the

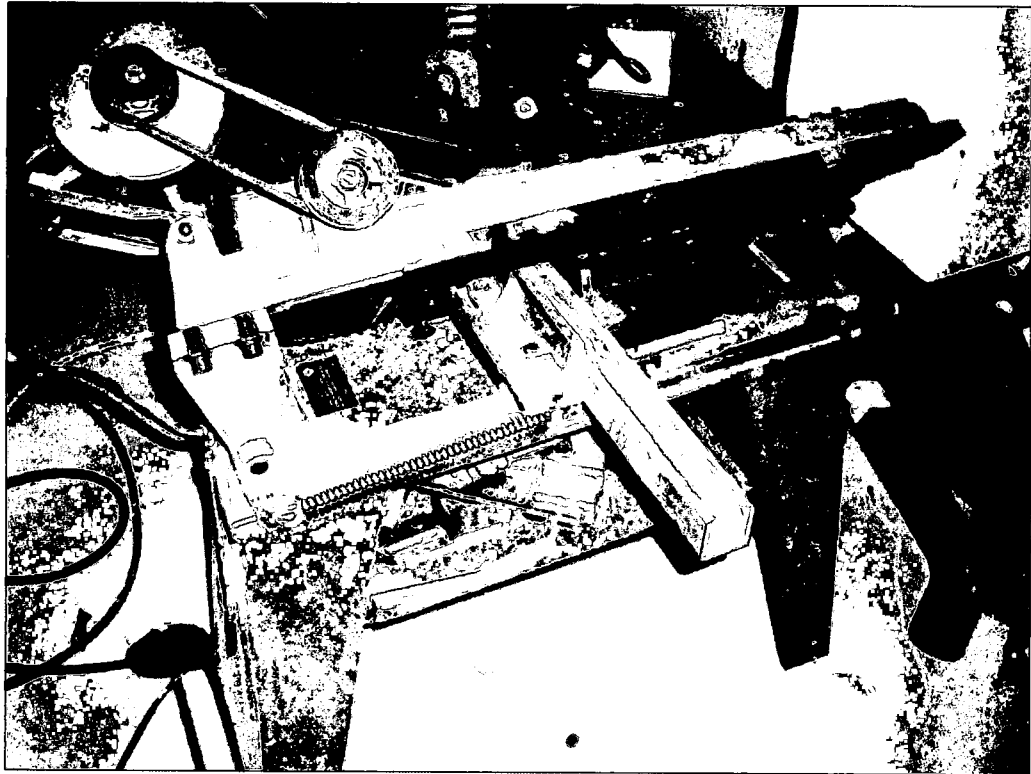


Figure 8 Cutting of aluminum stock for optical bench stand

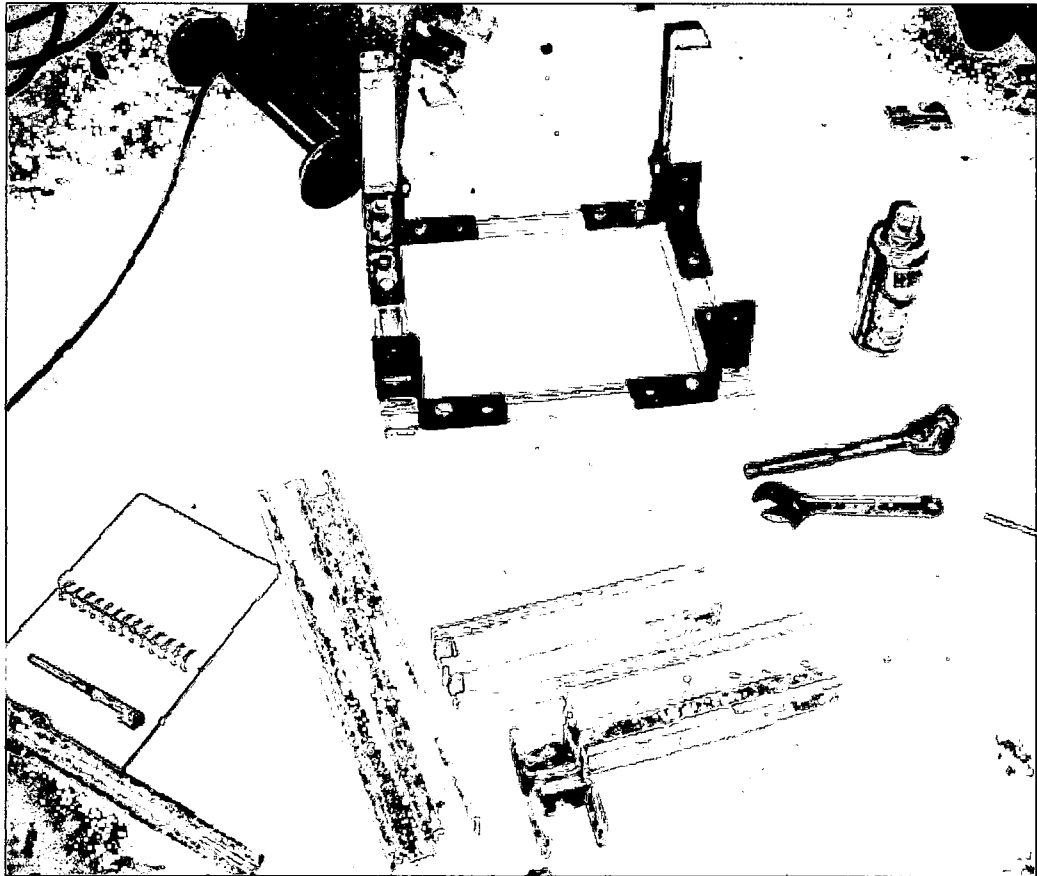


Figure 9 Optical bench stand assembly

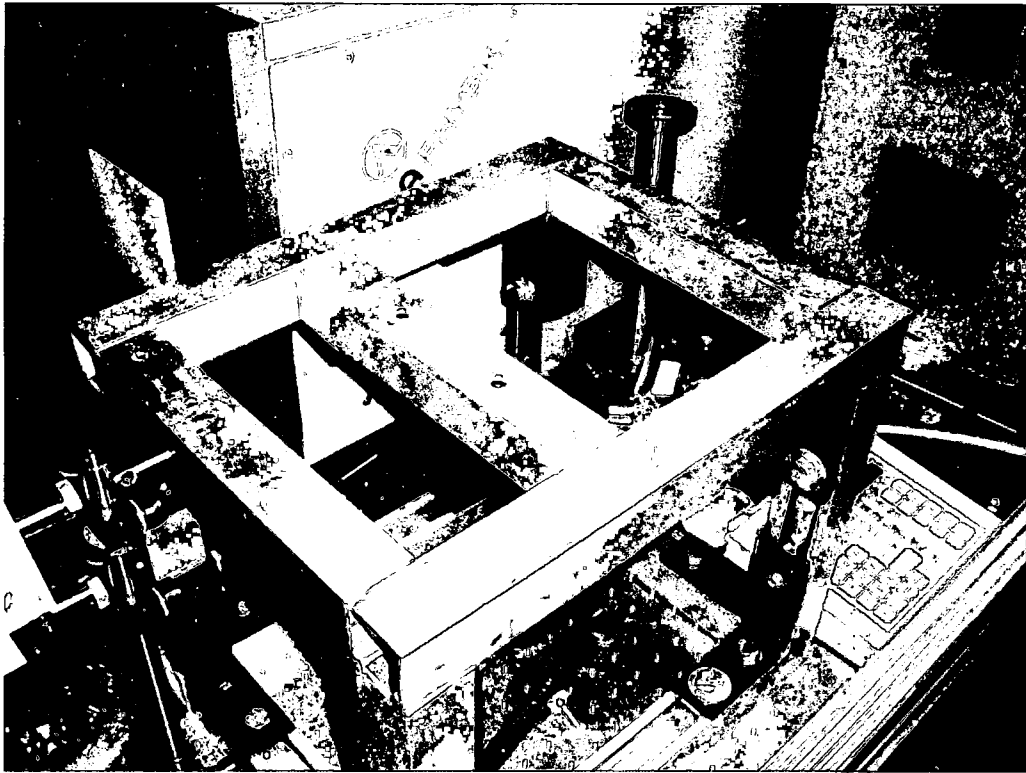


Figure 10 Mounting stand to optical bench

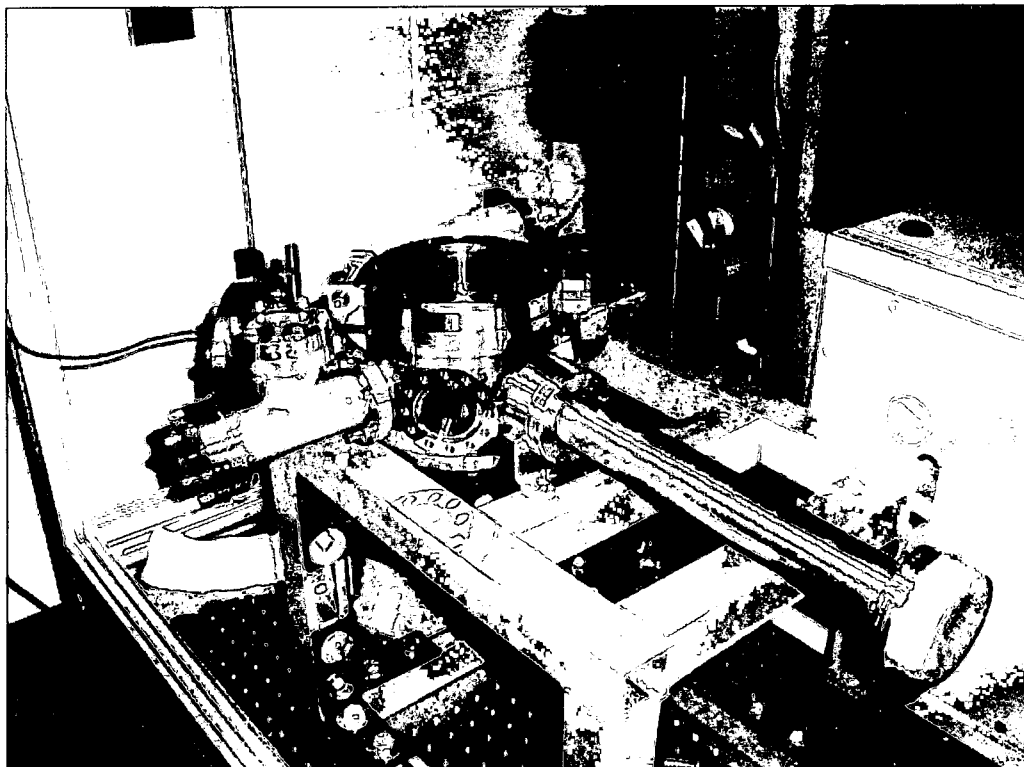


Figure 11 Assembly of the reaction chamber

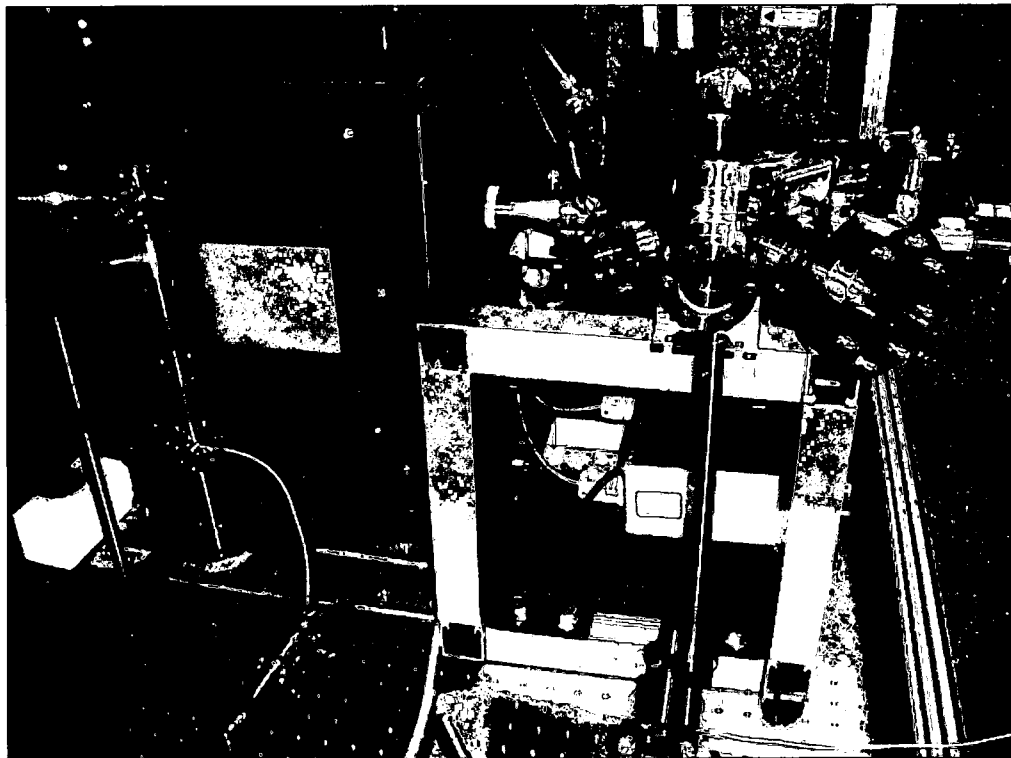


Figure 12 Reaction chamber nearing completion

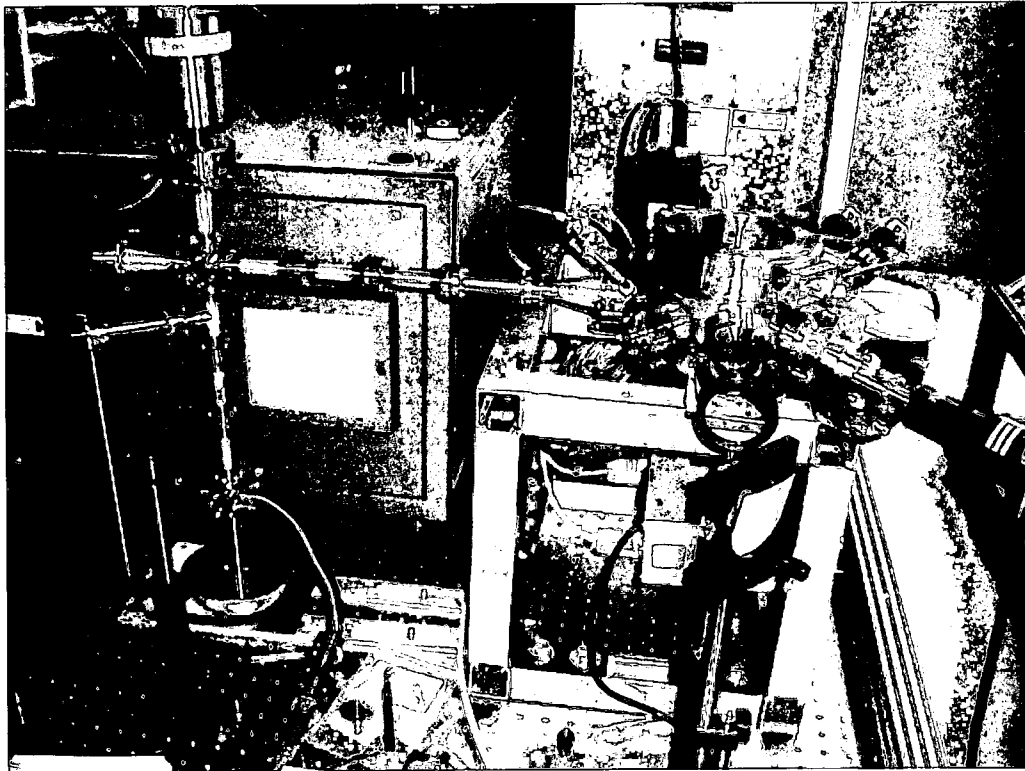


Figure 13 Completed reaction chamber on optical bench stand

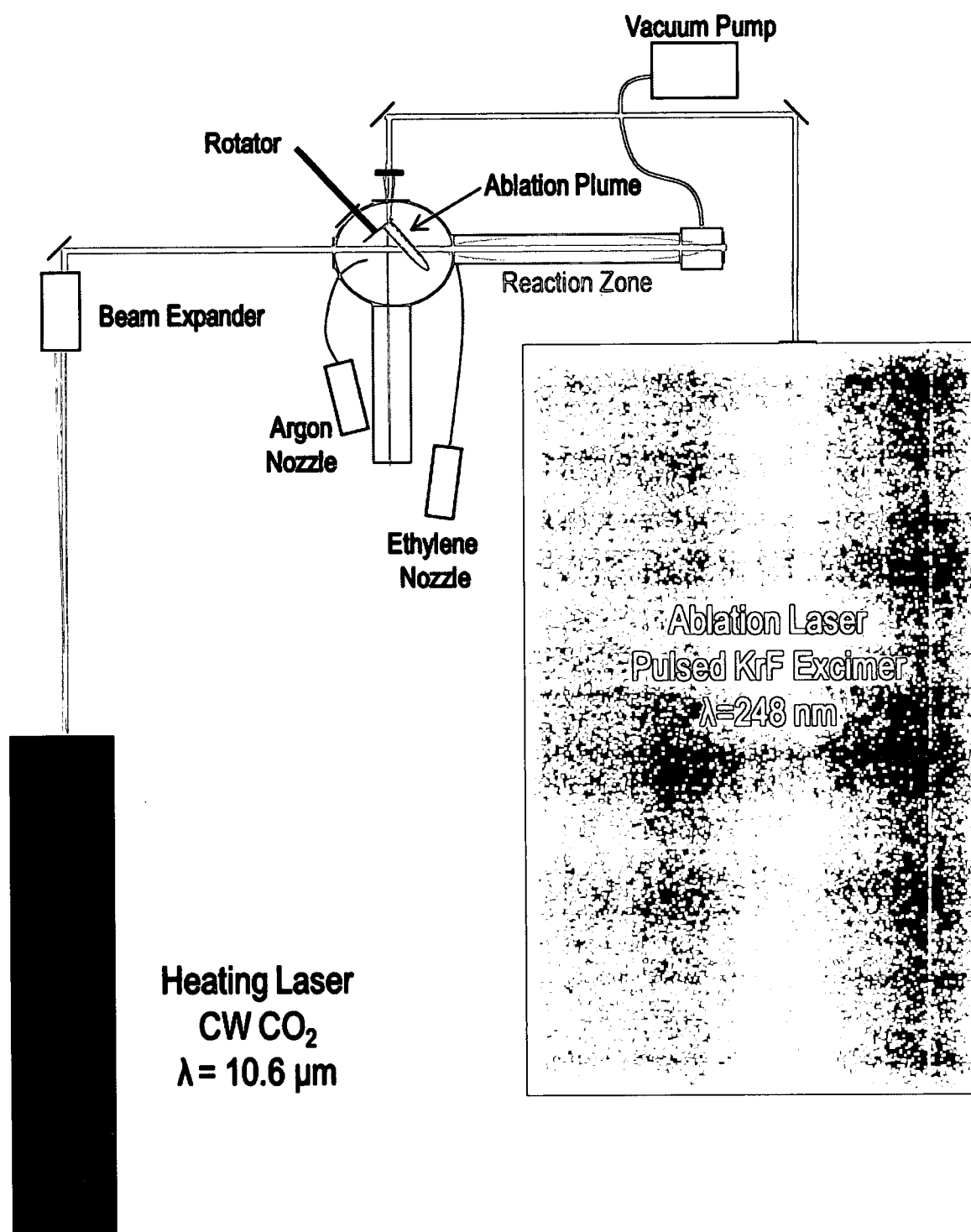


Figure 14 Layout of the experimental apparatus

material normal to the surface of the disk. The target is positioned so that the laser plume travels towards a long extension tube through which a Synrad 'Duo-Lase' continuous wave 30 W CO₂ ($\lambda = 10.6 \mu\text{m}$) laser propagates.

A mirror based beam expander, model 5XC6-36, from Space Optics Research Laboratories Inc., was placed between the Synrad CO₂ laser and the reaction chamber. Its purpose was to increase the size of the beam from less than 1 mm in diameter to 2.5 mm in diameter. This was done to increase the probability that particles and hydrocarbon gas traveling through the extension tube would be heated by the laser beam. Hydrocarbon and inert gas insertion was optimized with a Hastings[®] Model 400 Power Supply and Teledyne/Hastings[®] mass flow controllers with a range of 0-500 SCCM. The chamber utilizes a Franklin Electric vacuum pump for evacuation with a 2" MDC[®] angle valve for vacuum control.

Pressure in the chamber was monitored by a MKS Baratron[®] capacitance manometer model number 627B11TLC1B. A throughput for rotational manipulation of the catalyst target inside the chamber was required. A model BRM-133-01 motorized, graduated rotator from MDC[®] was located and installed into the chamber. A custom extension for the rotational manipulator was also needed to properly locate the target inside of the chamber. It was CAD designed in Solid Works[®] and subsequently CNC machined from stainless steel by Mound Manufacturing Inc. Dayton, OH. A diagram of the rotator extension is located in Figure 15. An image of the fused silica disk with a nickel thin film mounted to the rotator extension is located in Figure 16.

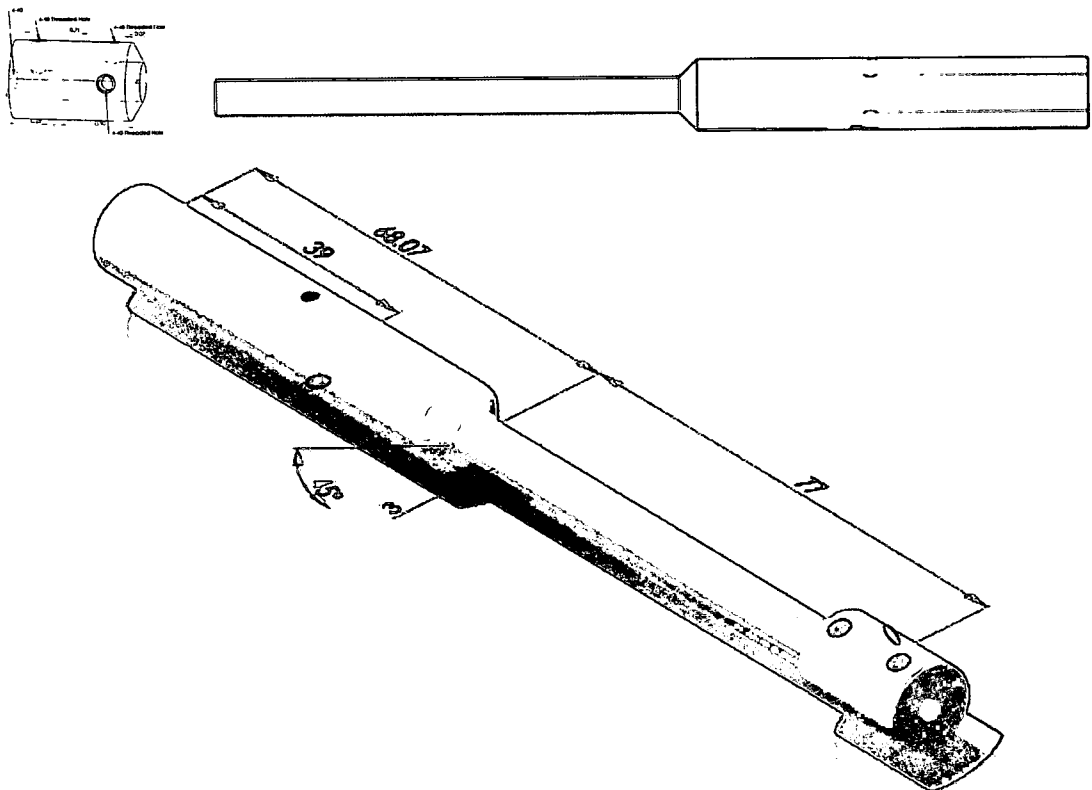
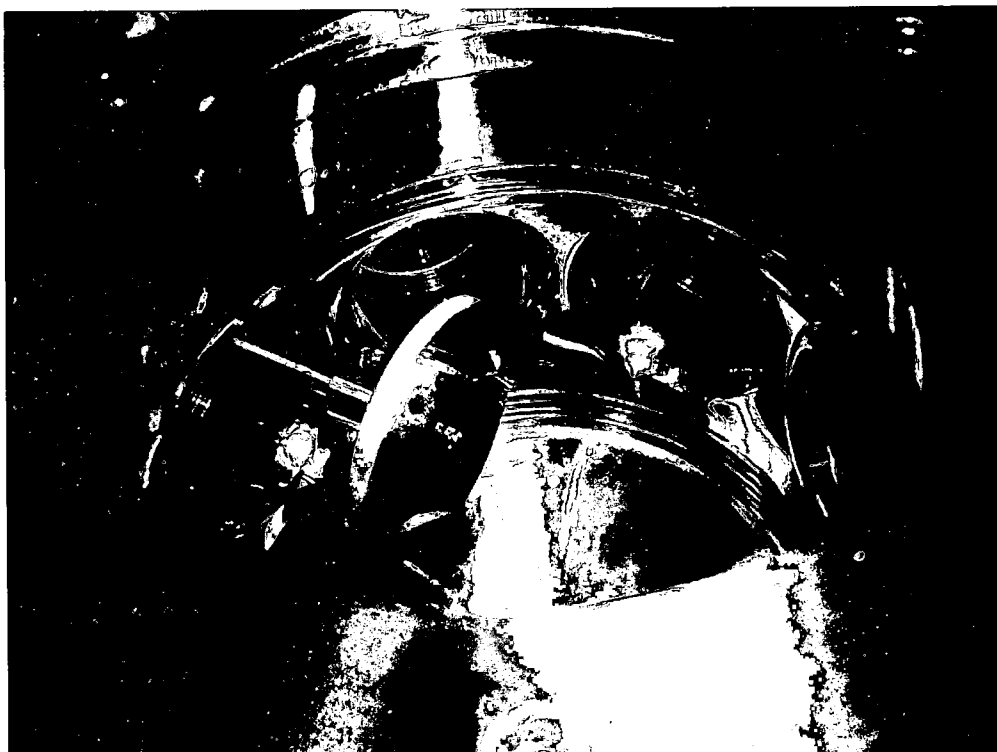


Figure 15 Diagram of CAD designed rotator extension



**Figure 16 Fused silica disk with nickel thin film mounted
to rotator extension inside reaction chamber**

2.2 Experimental Procedure

The task was to prepare a 5 cm diameter fused silica disk for deposition of a metal thin film. The disk was thoroughly cleaned to remove all traces of contamination and ensure proper adhesion of the thin film. A mixture of 50/50 hydrofluoric acid/water is used to ensure removal of remaining catalyst from previous experiments. The disk is then quickly rinsed with water to limit etching of the fused silica by the HF acid. The substrate is then rinsed with acetone, air dried and placed in the plasma sputtering chamber for deposition.

The sputtering chamber was pumped down to 3×10^{-6} Torr with a mechanical vacuum pump working in concert with a Turbotronik[®] turbo vacuum pump using a NT 20 controller. Once the chamber has been adequately evacuated, argon flow is introduced into the chamber until a steady state pressure of 18 mTorr is realized. The presence of argon is twofold, it flushes out traces of oxygen and nitrogen while providing a medium to ionize and carry catalyst ions to the substrate. The plasma is generated with an RF Power Products[®] RF5S power source while the rate of deposition is monitored by a quartz crystal microbalance within the deposition area. Measurements taken by the microbalance are fed into an Inficon[®] deposition monitor with stored calibrations for catalyst materials frequently deposited. A photograph of a Ni thin film deposition in progress can be seen below in Figure 17. Once the desired film thickness is achieved, the RF source and vacuum pumps are turned off and the argon gas flow is increased to bring the chamber up to atmospheric pressure.

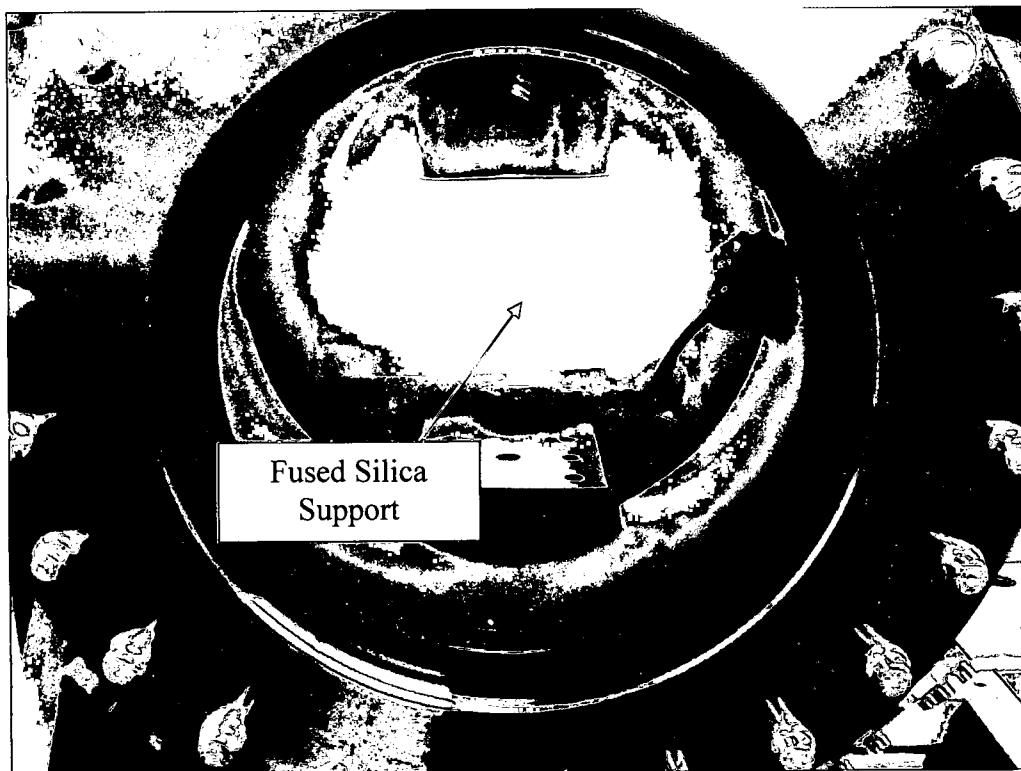


Figure 17 Nickel thin film deposition in progress

The disk with the thin film on the surface is then removed and placed into the reaction chamber and attached to the rotator extension.

Holey Carbon TEM grids and 1"x1" silicon wafers were thoroughly cleaned and inserted into the chamber to collect materials as they flowed through the system. Material was collected in four positions inside the reaction chamber. A diagram of the sample collection points is located in Figure 18. These collection points corresponded to critical points along the path of the floating nanoparticles. This was done to investigate the different aspects of the growth process; ablation, catalyst particle formation, carbon shell nucleation and tube growth.

The first sample collection position was onto a 1"x1" silicon wafer located directly across from the ablation target at a distance of 3". This was done in order to evaluate the size and morphology of the catalyst particles generated from the ablation plume.

The second collection point was inside the extension tube directly after injection of the hydrocarbon gas. The purpose of evaluating samples from this location was to look at particles that were in the reaction zone for a short period of time. Both a silicon wafer and Holey Carbon TEM grids were placed at position two which is 5.25" from the ablation target.

The third collection point was at the end of the laser propagation tube at a distance of 20.5 inches from the ablation target. Due to size constraints, there is only enough room for a TEM grid attached to a stainless steel strip. This strip

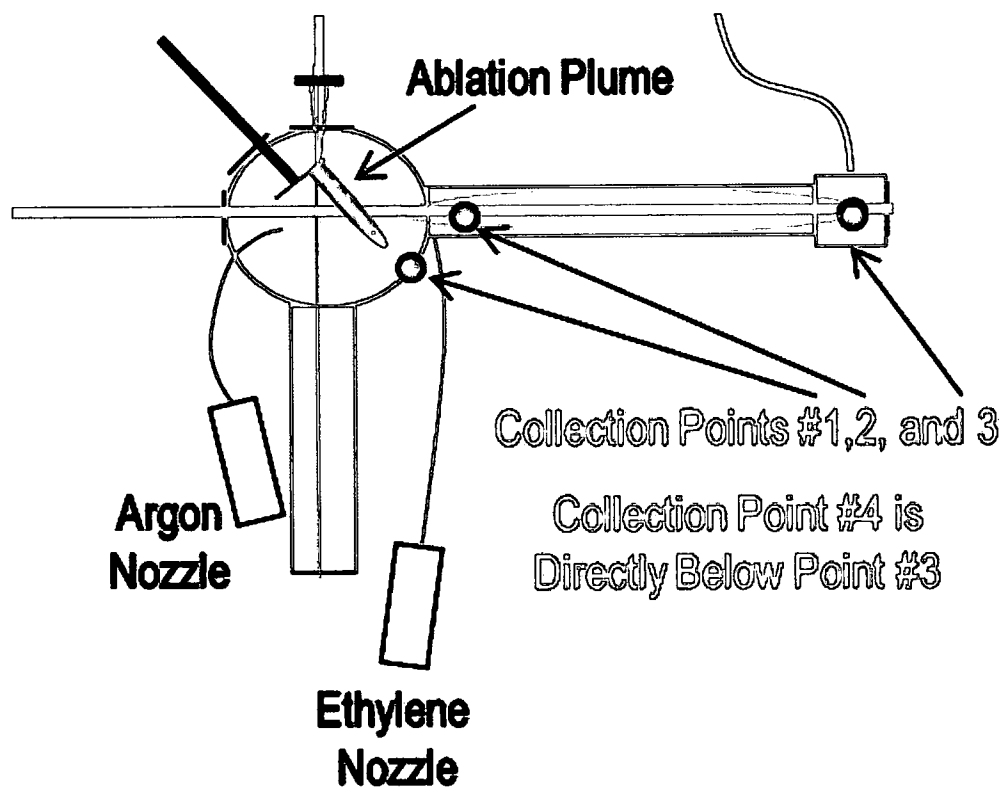


Figure 18 Sample collection points

was suspended directly below the path of the heating laser. Collection is done at this point to evaluate how much growth has occurred from position two to position three and represents the maximum amount of growth that is possible in the reaction zone.

The fourth collection point is onto a silicon wafer just before the port leading to the vacuum valve. Samples were collected at this point due to size constraints at position three.

2.3 Description of Experiments

The first experiment, experiment #0, was performed to evaluate the overall performance of the reaction chamber. The chamber was pumped down and tested for leaks until a pressure of 62 mTorr was realized. Maps of pressure versus mass flow rate were created to evaluate the mass flow contribution to the environment. These plots are located in Figures 19, 20 and 21. The original proposal was to leave the vacuum valve fully open using controlled insertion of gases to regulate the pressure. This would have been the most accurate way to control pressure but the maximum attainable pressure with this configuration was 4.1 Torr. This meant that the vacuum valve would have to be partially closed to obtain pressures greater than 4.1 Torr or if mass flow rates less than 500 SCCM for argon or ethylene were desired.

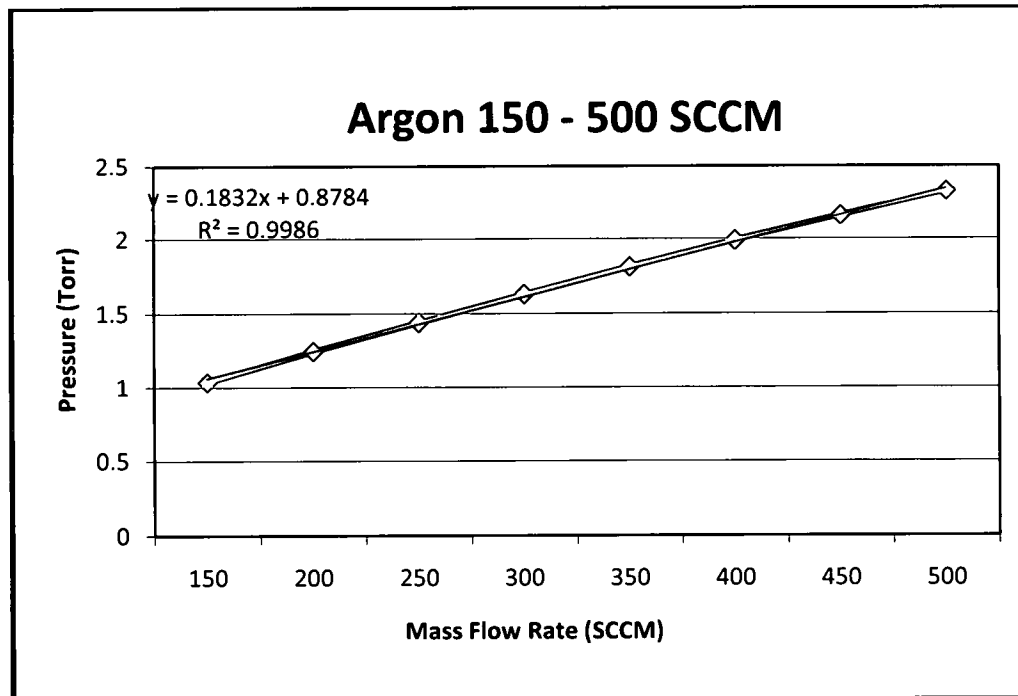


Figure 19 Pressure vs. argon mass flow rate

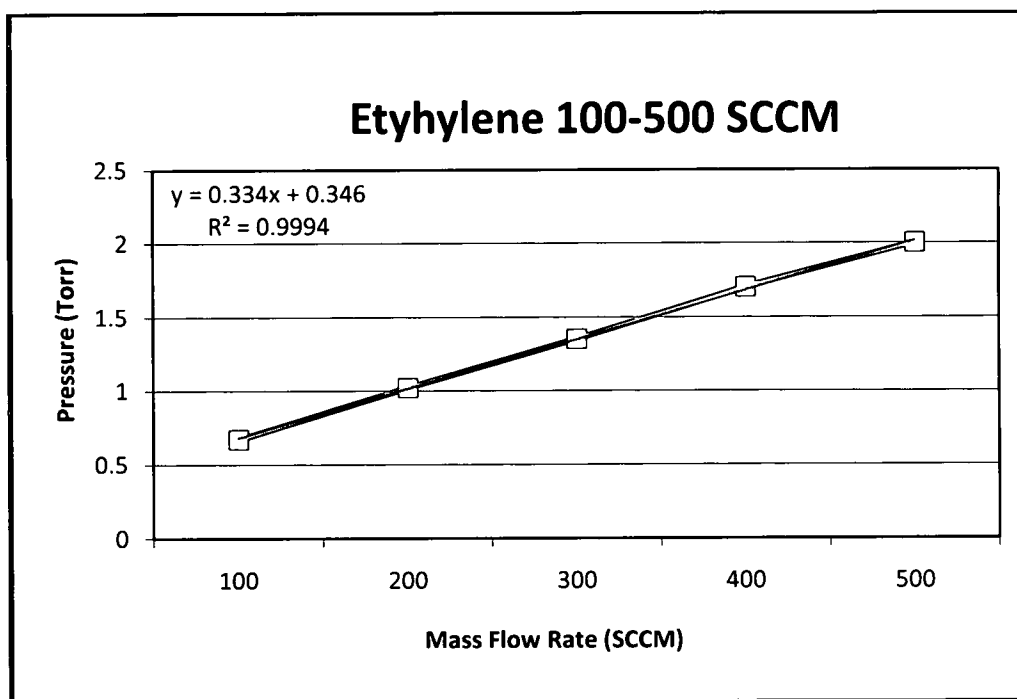


Figure 20 Pressure vs. ethylene mass flow rate

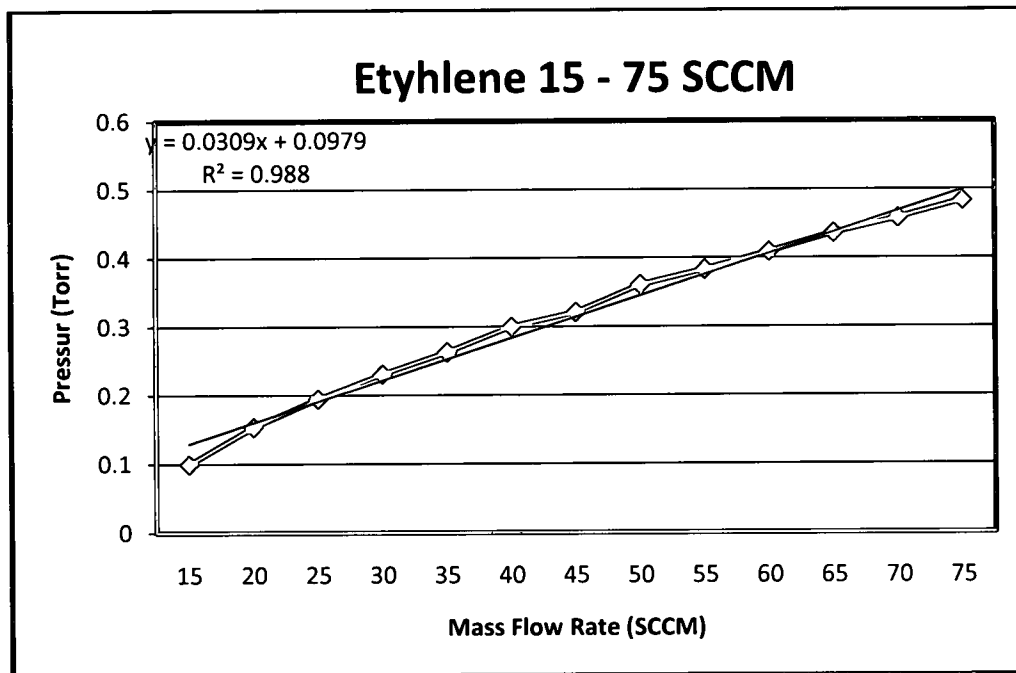


Figure 21 Pressure vs. ethylene mass flow rate

For experiment #0 a pressure of 3.5 Torr was realized with mass flow rates of 500 SCCM argon and 406 SCCM for ethylene. The pressure was taken up to 8 Torr by turning down the vacuum valve and allowing the chamber to reach steady state. The CO₂ heating laser was aligned and propagated through the chamber at 75% power while a 50 nm iron target was used to verify focus of the laser and evaluate ablation characteristics. Photographs of the thin film before and after ablation are located in Figure 22. Video of the plume was captured with a model GRD271US JVC® mini DV camcorder. A single frame from the ablation video is located in Figure 23. It was hypothesized that optical emissions from nanoparticles being energized by the heating laser might be observed, but none were found at that time.

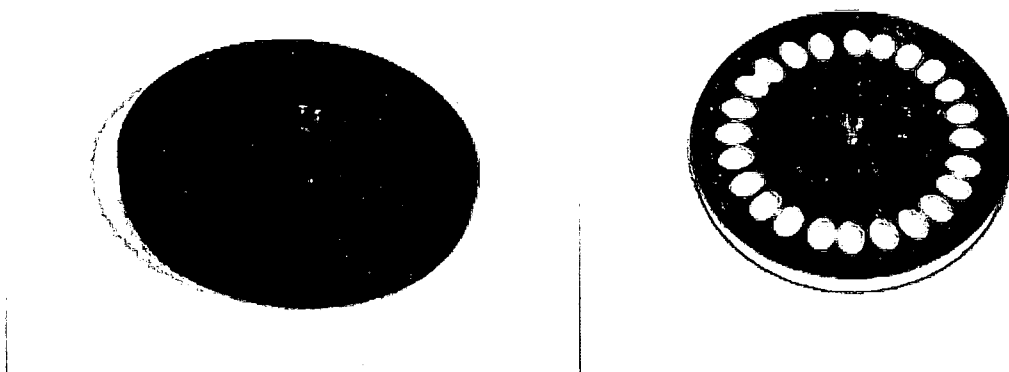


Figure 22 Nickel thin film before and after ablation



Figure 23 Ablation plume from experiment #0

Experiments #1, 2 and 3 were done to study the effect of laser intensity on growth. Laser power levels of 85%, 20% and 50%, respectively, were used. Unfortunately, the usefulness of these experiments was reduced when it was discovered that the ethylene mass flow rate was much too high.

Experiment #4 was done in order to evaluate the effect of reduced hydrocarbon concentration. The ethylene mass flow rate was reduced to 75 SCCM while the argon flow rate was held constant at 498 SCCM. CO₂ laser power was set at 50%, giving an average power of 13.5 W inside the chamber.

Experiments #5 and #6 were conducted to determine the contribution of the heating laser. Both experiments were completed with ethylene mass flow rates of 50 SCCM but experiment #5 was completed without propagating the heating laser through the chamber while experiment #6 was performed at 50% laser power.

Questions still remained about the mechanism through which growth was occurring. In order to better understand the contribution of the CO₂ heating laser, the ablation laser was not used for experiment #8 and a sample of CNTs was flowed through the chamber with the CO₂ laser running at 50% power. To do this, the sample of CNTs was placed in front of the argon insertion nozzle and the chamber was pumped down. Once properly evacuated, the ethylene mass flow rate was set to 50 SCCM while the argon was set to 498 SCCM. Once the argon flow was turned on, nanotubes began floating through the chamber and down the extension tube.

Before the next experiment was conducted, the size of the CO₂ laser beam was taken into consideration. At 2.9 mm the beam was clearly smaller than the inside diameter of the extension tube inside diameter of 25 mm. This gave a low statistical

probability that particles were being heated uniformly as they traveled through the reaction zone. In order to increase that probability it was determined that the beam size needed to be increased. A lens based beam expander was considered for this task; unfortunately these optics can be quite costly. After further investigation, the intrinsic divergence of the Synrad CO₂ laser beam was found to be 4 mrad [64]. Meaning that for every meter of distance the beam travels it diverges 4mm in diameter. Beam size measurements were subsequently made in light of this information. Beam divergence was found to be approximately 2.5 mrad, significantly less than the manufacturers stated value. This knowledge, however, was used to increase the beam size without additional optics by moving the CO₂ laser and power supply 0.5 meters away from the reaction chamber. The beam expander was then moved 0.25 meters closer to the chamber in order to maximize divergence in the available space. This increased the beam size entering the beam expander to approximately 2.5 mm without additional optics. This increased the output diameter from the mirror based beam expander to approximately 5.0 mm. Unfortunately, the increase in beam size came at the expense of a reduction in power density by a factor of 3.

Experiment #8 was performed to evaluate the effects of higher pressure on the reaction as well as determine if the expanded beam size was useful for generating more homogenous products. The maximum measureable pressure of the MKS Baratron[®] capacitance manometer was 10 Torr so a pressure of 9.6 Torr was determined suitable. CO₂ laser power was set at 95%, the maximum attainable with the Synrad[®] Duo Lase. Extra caution was used during the experiment due to the dangers of lasing at these high power levels.

The final experiment, experiment #9, was conducted with an ethylene mass flow rate of 25 SCCM, the lowest stable flow rate with the mass flow controllers being used. This was done to further decrease the hydrocarbon concentration and allow for analysis of the effects at lower pressure. The optimum pressure for nanoparticle formation is 1 Torr when using the TTFA method. In order to approach that pressure the argon mass flow rate was reduced to 375 SCCM as well. With the vacuum valve fully open a steady state pressure of 1.90 Torr was realized. Table 1 contains a summary of all the experiments performed for this effort.

Experiment #	Catalyst	Catalyst Thx.	Pressure (torr)	Mass Flow Rate		Laser Power	
				Argon	Ethylene	CO2 (CW)	Excimer (Pulse)
0	Fe	50 nm	3.5- 8.0	406	500	75%	560 mJ
1	Fe	50 nm	3.5	406	500	85%	559 mJ
2	Fe	20 nm	3.5	406	500	20%	557 mJ
3	Ni	20 nm	5.02	497	501	50%	555 mJ
4	Ni	50 nm	8.08	498	75	50%	567 mJ
5	Ni	20 nm	5.09	498	50	N/A	555 mJ
6	Ni	20 nm	5.05	497	50	50%	555 mJ
7	N/A	N/A	7.2	498	50	50%	561mJ
8	Ni	20 nm	9.6	497	50	95%	567 mJ
9	Ni	20 nm	1.9	375	25	95%	505 mJ

Table 1 Summary of Experiments Performed

2.4 Characterization - Raman Spectroscopy

When a material is illuminated with intense monochromatic light specific vibrational modes occur at frequencies outside of the laser wavelength. These modes arise from optical phonon mode coupling, not from atomic species themselves. This becomes useful when characterizing homogenous material with different bonding types.

CNTs have strong vibrational modes in the Raman bands that can be easily detected and plotted according to their intensity. Raman spectroscopy is frequently employed to characterize carbon nanotubes. One of the defining peaks, the D-peak, is found near 1300 cm^{-1} . The intensity qualitatively corresponds to the amount of amorphous carbon and disorder present in sp^2 bonds [8]. The G-Peak indicative, of the E_{2g} vibration of hexagons, is located at 1582 cm^{-1} . Purified SWNTs, being graphitic in nature, are found between $8\text{-}15\text{ cm}^{-1}$ lower than pure graphite [65] due to strain induced from bending graphite into small diameters. The diameter of a carbon nanotube can also be determined with Raman spectroscopy. The shift of the Radial Breathing Modes (RBM) is proportional to the inverse of SWNT diameters and follows the equation [66].

$$\omega_{RBM}(\text{cm}^{-1}) = \frac{223.5}{d+12.5}$$

Where d is the diameter in nm.

Chapter 3

Results and Discussion

3.1 Results

A Renishaw inVia Raman microscope was used with a 633 nm laser to gather spectra. Some particles from experiment #1, #2 and #3 were visible with the 50x objective on the microscope. The largest particles obtainable were characterized in order to ensure illumination of the sample material and not of the background. This was also beneficial for getting a higher signal to noise ratio. Spectra from all three samples had broad D-peaks at 1300 cm^{-1} indicating amorphous carbon with no other carbon peaks observed. Spectral scans were performed from $0\text{-}400\text{ cm}^{-1}$ in search of peaks indicating CNT RBMs but none were found. The lack of a G-peak near 1600 cm^{-1} was an indication that the hydrocarbon concentration was in gross excess. TEM micrographs were obtained with a Philips CM 200 using a LaB_6 filament that confirmed this suspicion. The catalyst nanoparticles observed were fully encapsulated with thick carbon shells which fully inhibited nanotube growth. A representative Raman spectrum and micrograph of the sample material is located in Figure 24. The thick carbon shells can be seen in Figure 25 where the carbon shell was measured at 38 nm while a 41 nm thick shell can be seen in Figure 26.

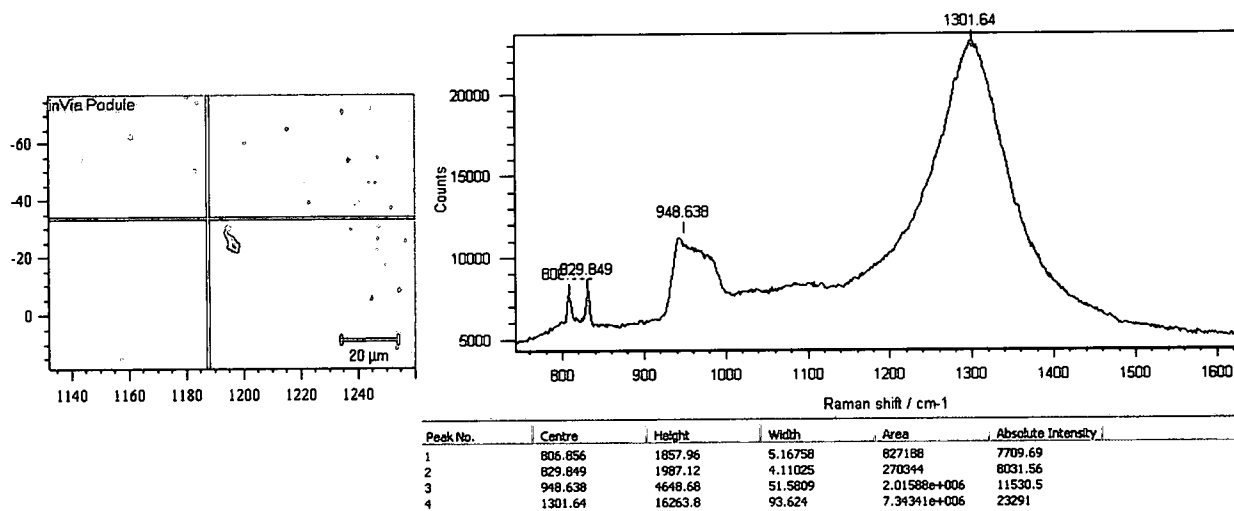


Figure 24 Photo micrograph and Raman spectrum from experiment #1

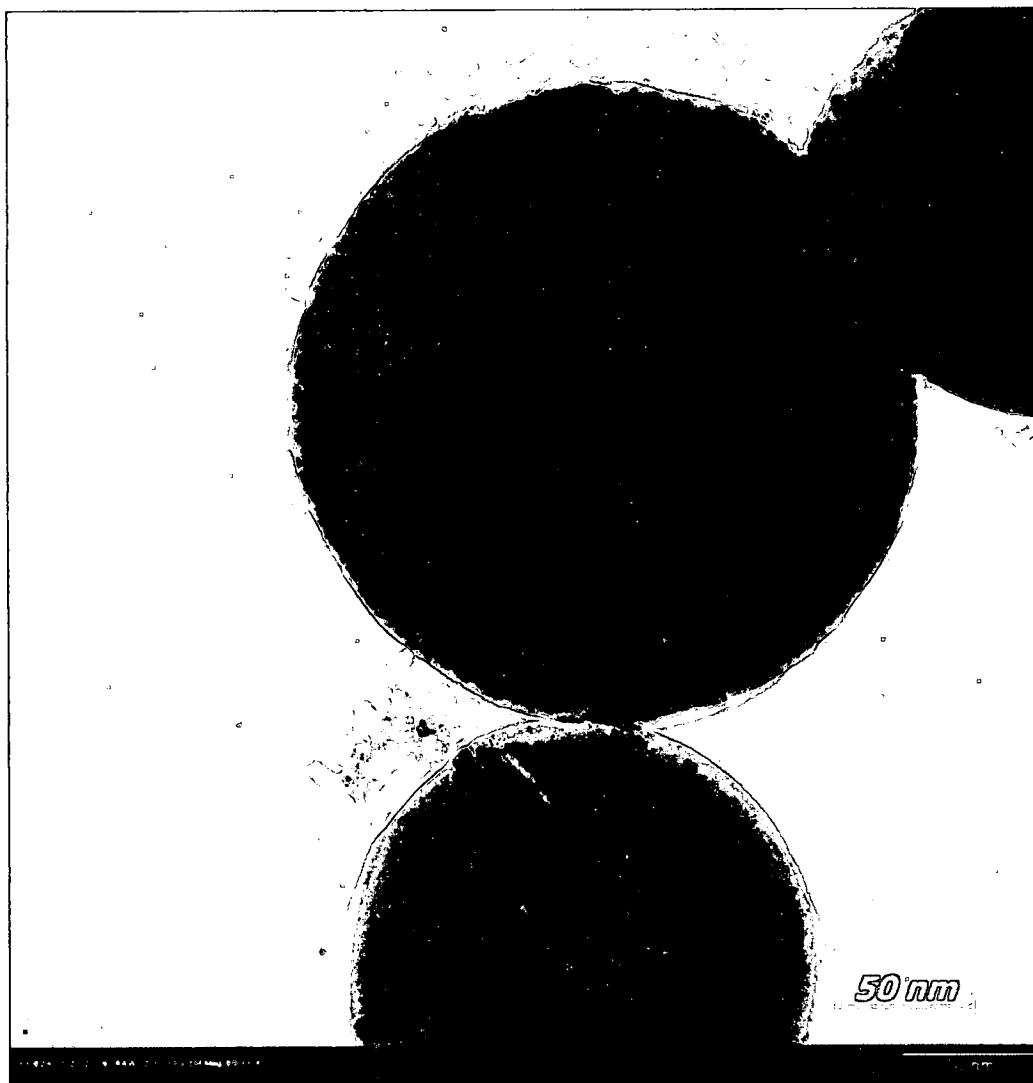


Figure 25 TEM micrograph of a 38 nm carbon shell from experiment #0

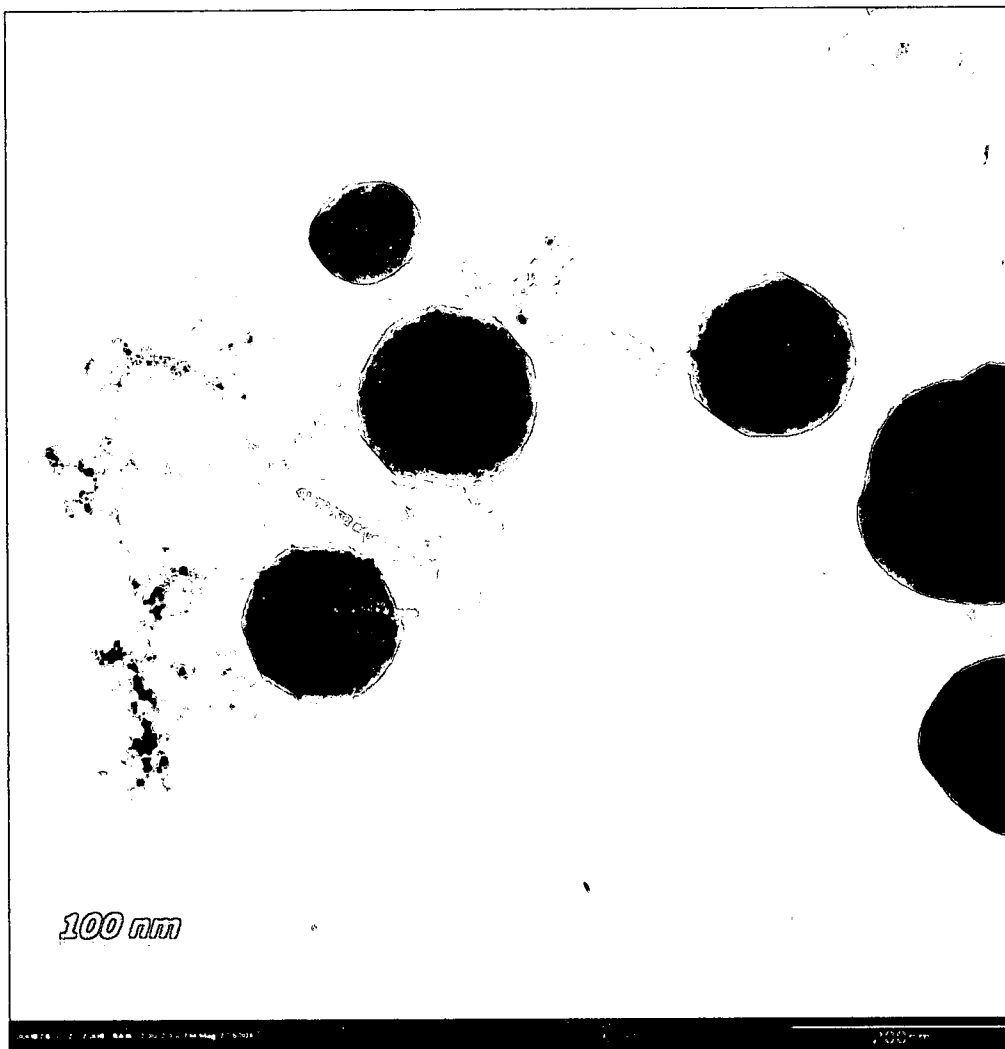


Figure 26 TEM micrograph of a 41 nm carbon shell from experiment #0

Knowing that the hydrocarbon concentration was much too high in the previous runs, the ethylene mass flow rate was substantially reduced from 500 SCCM to 75 SCCM for experiment #4. The Raman spectrum from this experiment, seen in Figure 27, shows both a D-peak and a G-peak near 1600 cm^{-1} . This was very encouraging even though the G-peak was broad and at the same relative intensity as the D-peak. The size of the carbonaceous materials viewed under the microscope objective see in Figure 28 was however very impressive, especially when one considers that these materials were collected from position #1. Particles generated from the laser pulse travel in a straight line to position #1 and merely cross the path of the heating laser. The time these materials spend in the reaction zone is estimated to be less than 100 microseconds. The thick carbon shells observed in previous micrographs were no longer present. Islands of carbon and partial encapsulation were commonly observed as in Figure 29. Large masses of carbonaceous material as seen in Figure 30 were observed as well. These masses however should not be dismissed. They frequently had interesting tube-like features protruding. An example of one of these features can be found in Figure 31. Further investigation of these regions revealed several large diameter CNTs protruding from the masses as well. These CNTs were frequently covered with amorphous carbon as seen in Figure 32. More CNT micrographs of this sample are located in Figures 33 and 34. After the presence of CNTs was confirmed, many additional Raman scans were performed looking for RBMs and definitive peaks at 1600 cm^{-1} . Unfortunately, neither was found. This brings the utility of Raman spectroscopy into question for this work. While the number of CNTs captured during an experiment is unknown, particularly since

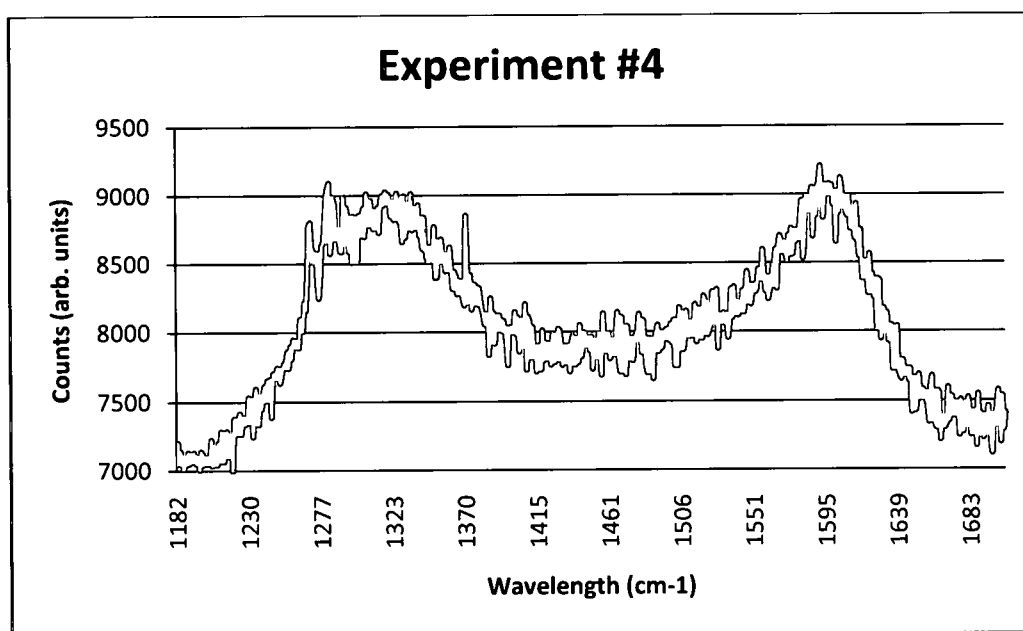


Figure 27 Raman spectrum from experiment #4

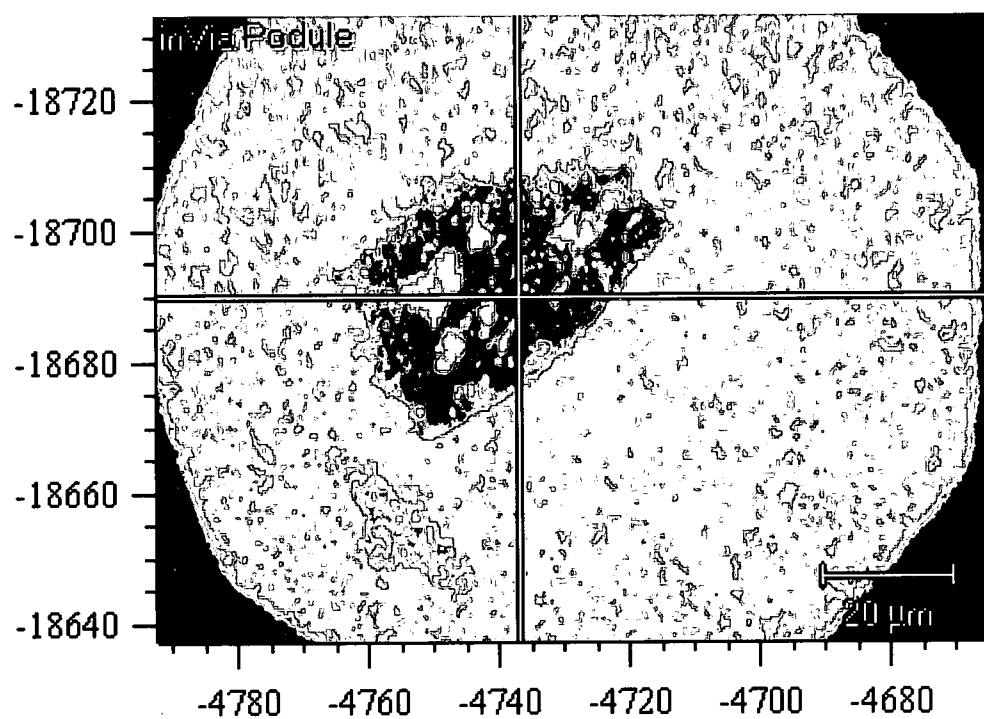


Figure 28 Photomicrograph of carbon specimen obtained from experiment #4

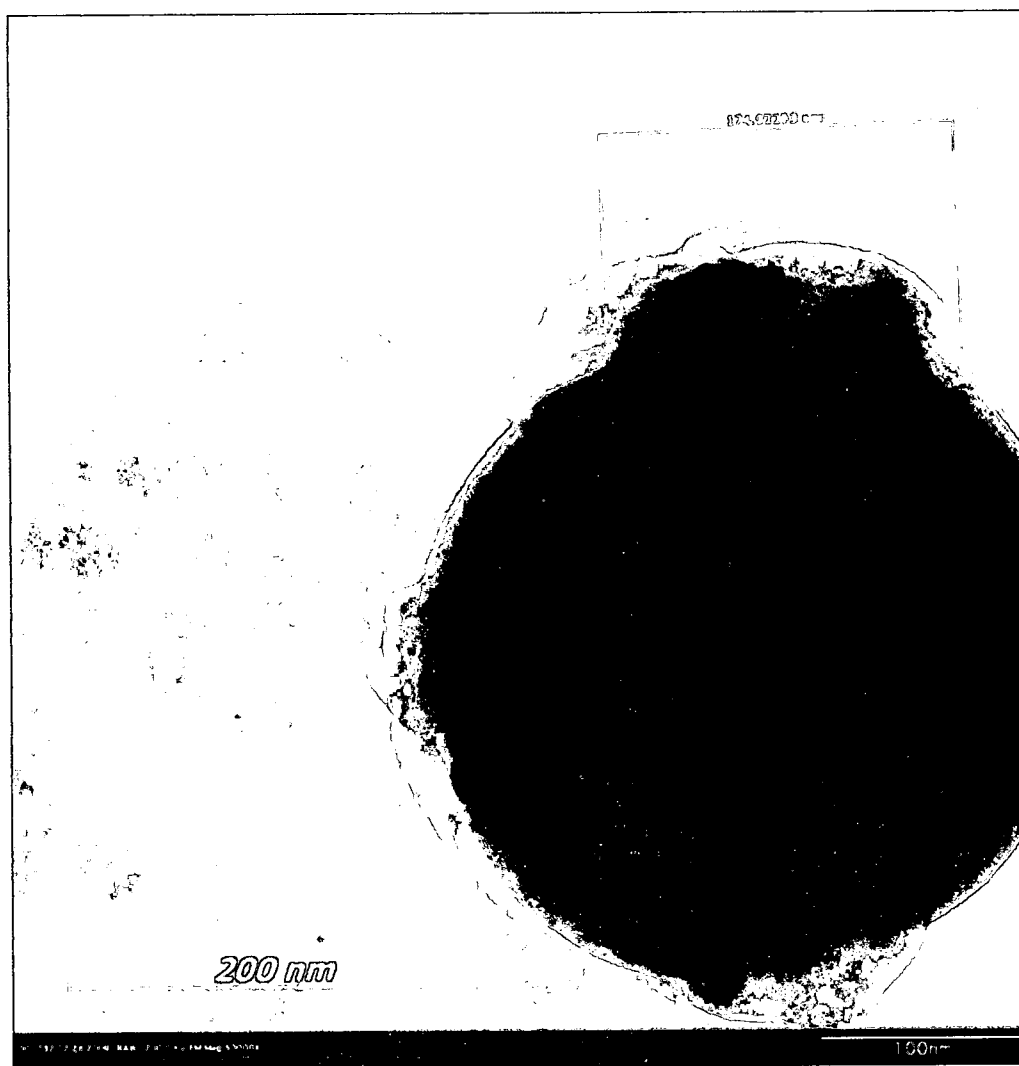


Figure 29 TEM micrograph from experiment #4 showing a large carbon island

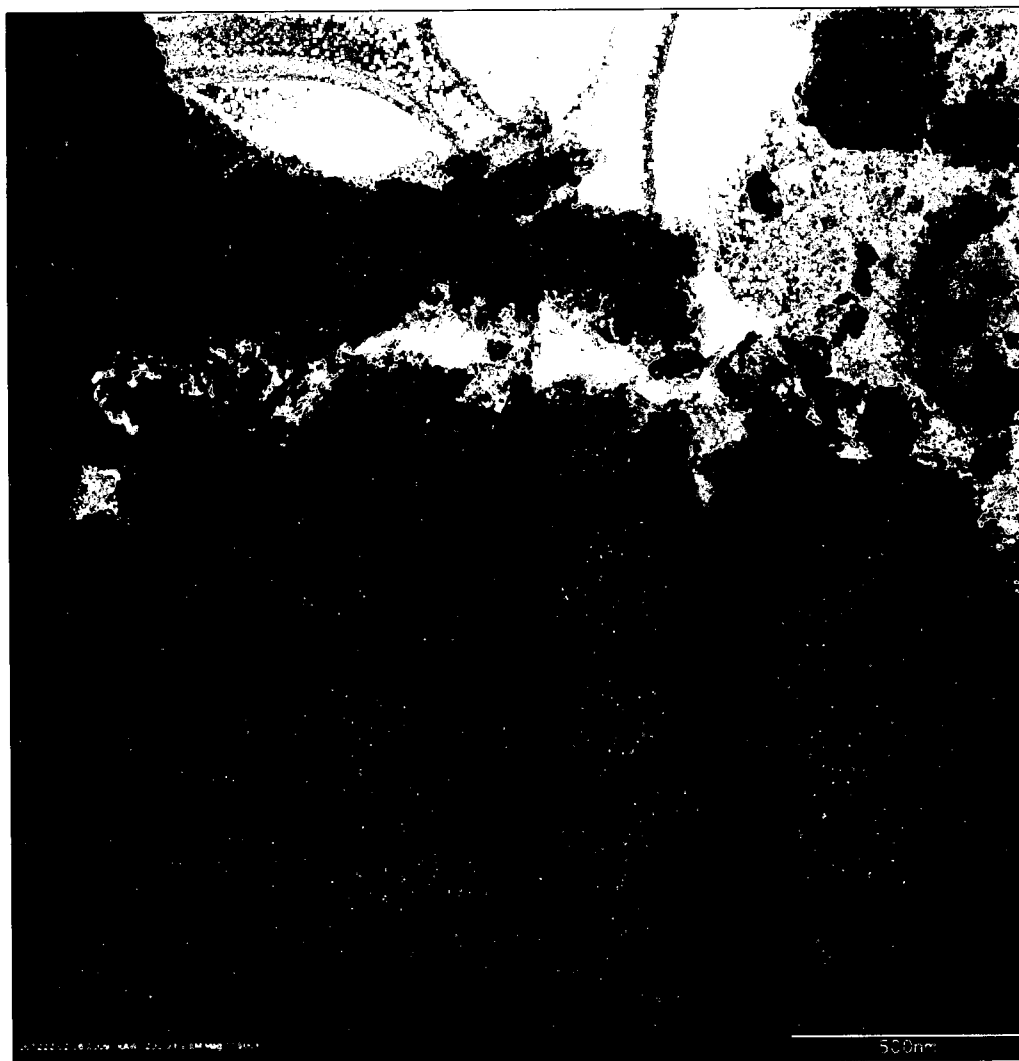


Figure 30 TEM micrograph from experiment #4 showing large carbon masses

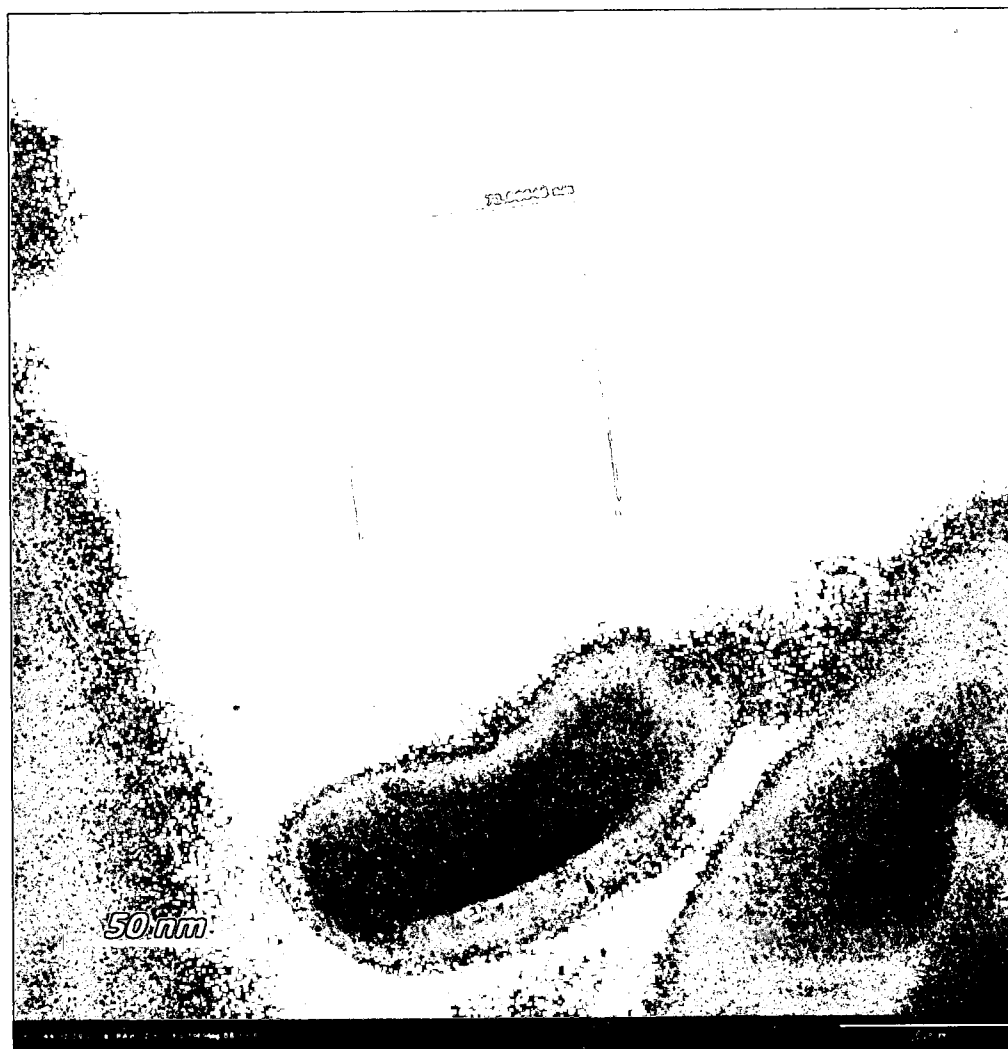


Figure 31 TEM micrograph from experiment #4 showing a 73 nm tube-like feature

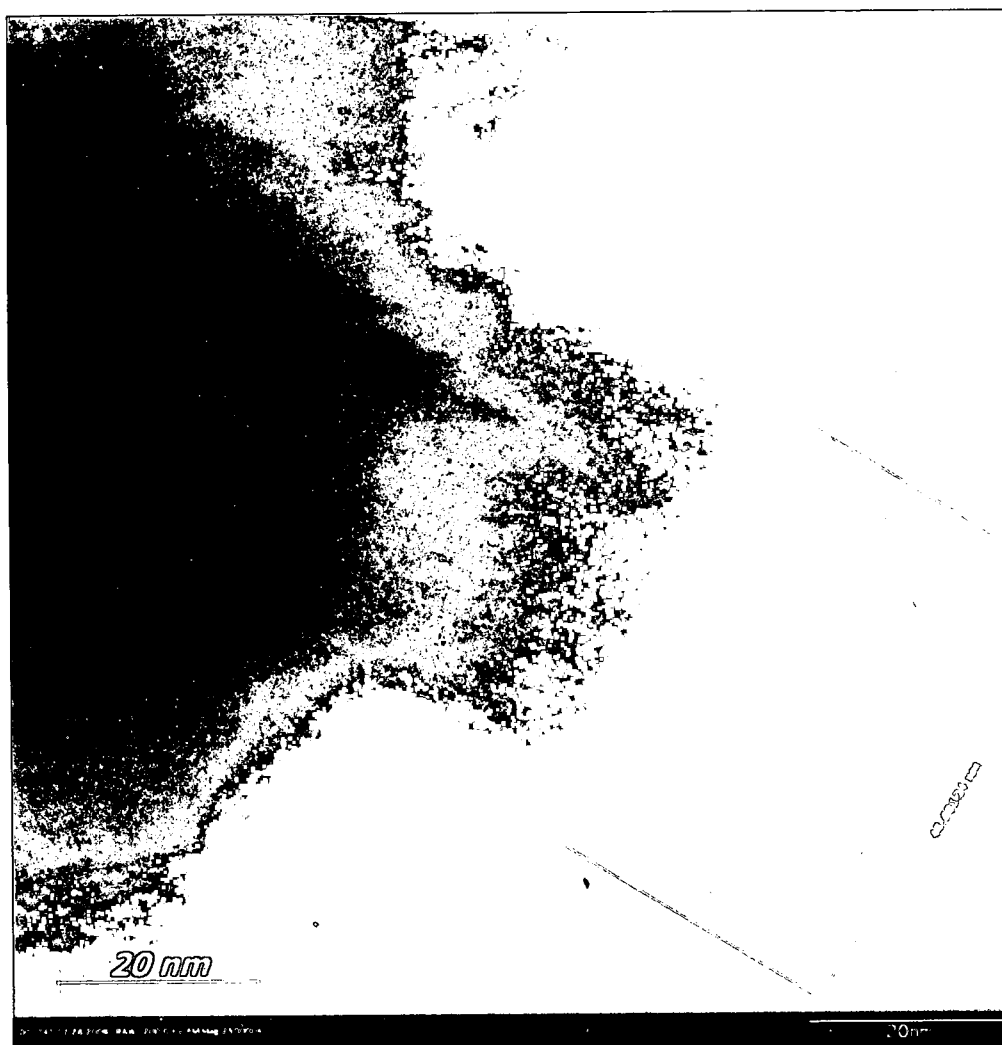


Figure 32 TEM micrograph from experiment #4 showing a 48 nm tube-like feature

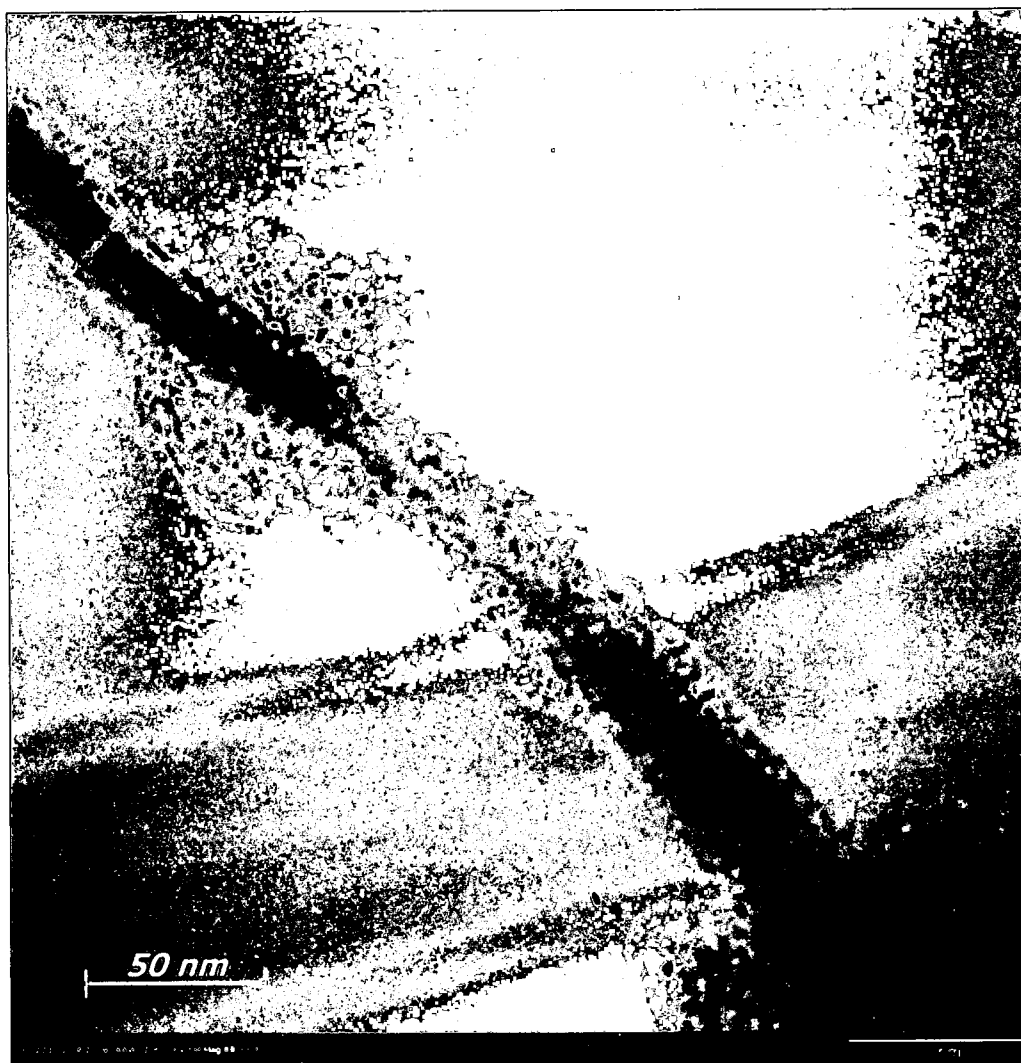


Figure 33 TEM micrograph from experiment #4 showing a 17 nm diameter CNT



Figure 34 TEM micrograph from experiment #4 showing a 21 nm CNT protruding from a carbon mass

the large masses may contain many more that could not be imaged, the population appears to be quite small. This makes the probability of gathering a clean CNT spectrum nearly impossible because there is no way to confirm that a given area will have CNTs present. This was particularly true when attempting to evaluate samples from positions #2 and #4 where the abundance of material was much lower. Additionally, the amorphous carbon that can be seen coating and partially encapsulating the CNTs is most likely overwhelming CNT spectra and damping characteristic vibrational modes.

Experiments #5 and #6 were conducted in order to determine the effectiveness of the CO₂ laser as a heating source. They were conducted without and with the CO₂ laser, respectively. A Raman spectrum from experiment #5 located in Figure 35 shows a very weak D-peak with the region of the spectrum around 1600 cm⁻¹ only slightly more intense than the background. No large particles were observed through the microscope objective as seen in Figure 36. This may have been part of the reason why the signal was so weak. The second run, experiment #6, revealed larger particles amidst the smaller particles. These can be seen in Figure 37. It is presumed that the larger particles were heated by the CO₂ laser and grew to greater sizes. The Raman spectrum obtained in Figure 38 shows a weak D-peak but a more intense, although equally broad G-peak.

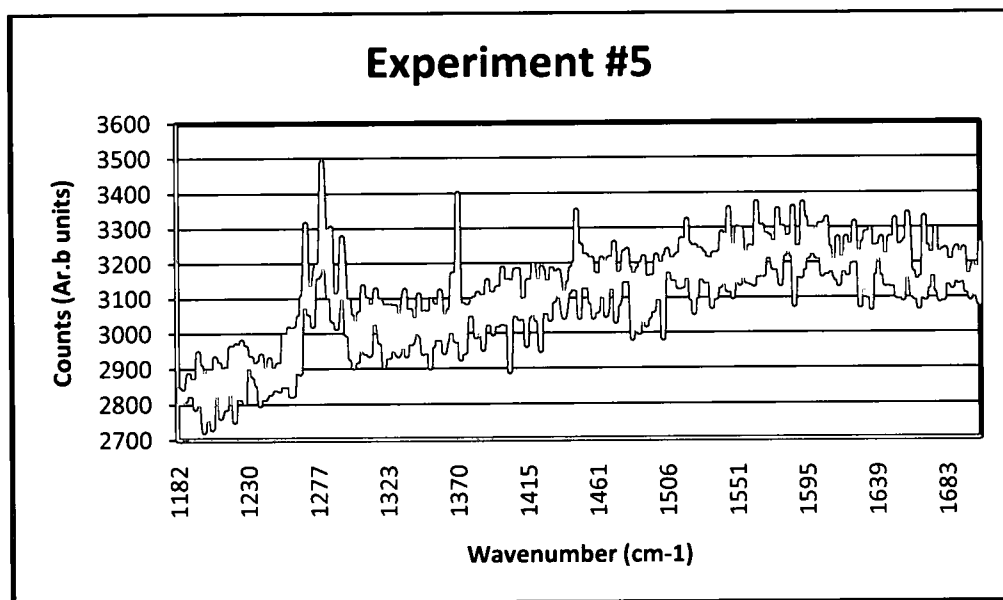


Figure 35 Raman spectrum obtained from experiment #5

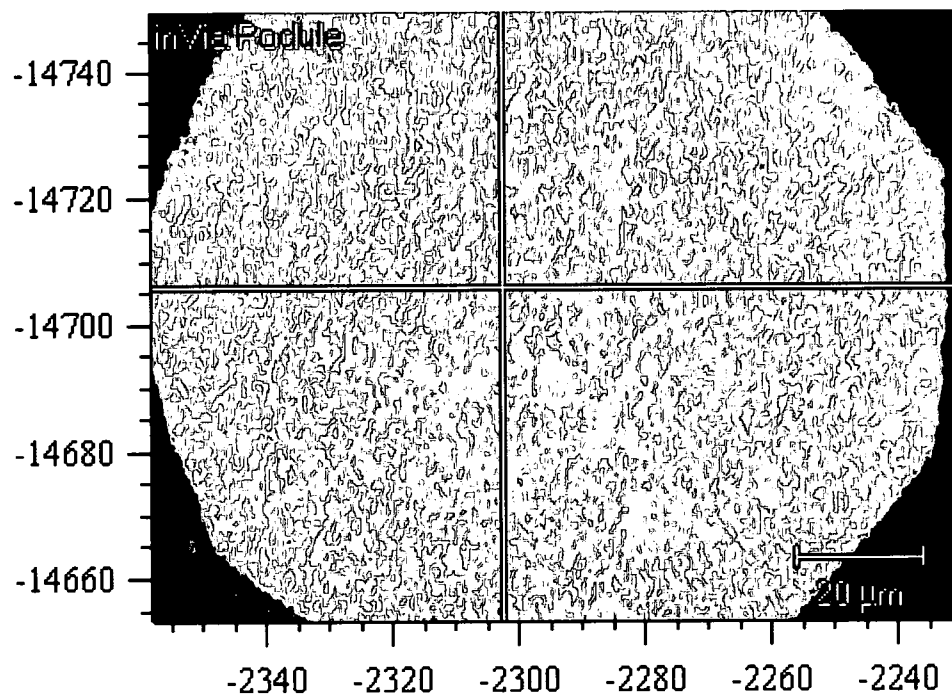


Figure 36 Photomicrograph of the material measured from experiment #5

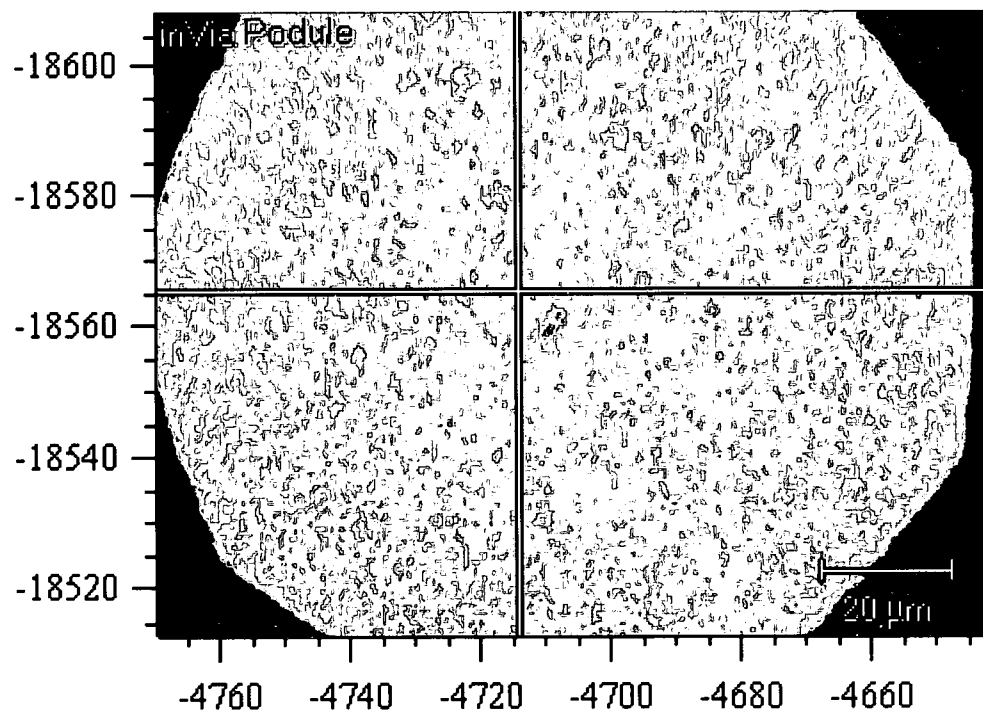


Figure 37 Photomicrograph of the material measured from experiment #6

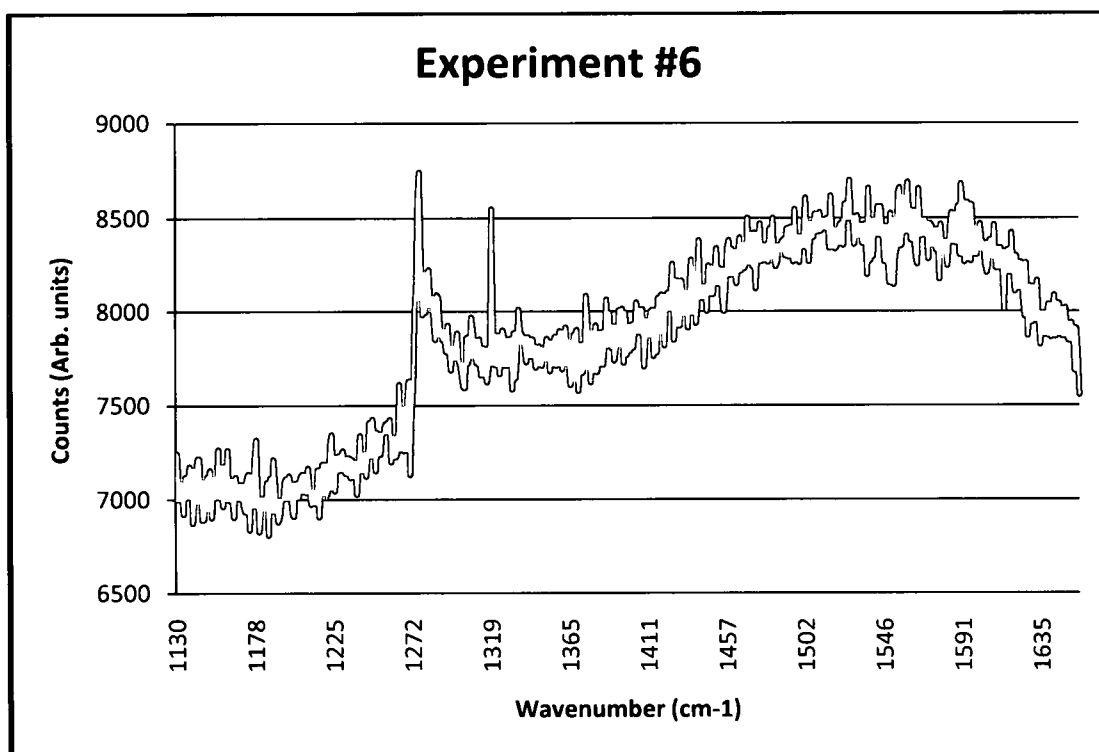


Figure 38 Raman spectrum obtained from experiment #6

For the purpose of comparison, SEM micrographs were taken at the same magnification with a Sirion[®] ESEM of samples collected from position 1. Qualitative measurements were taken of both Figure 39 and Figure 40. It seems probable that the particles from experiment #6 grew to larger sizes when they were heated by the CO₂ laser. While these micrographs were representative of the entire population, more work is required before measurements could be considered statistically significant.

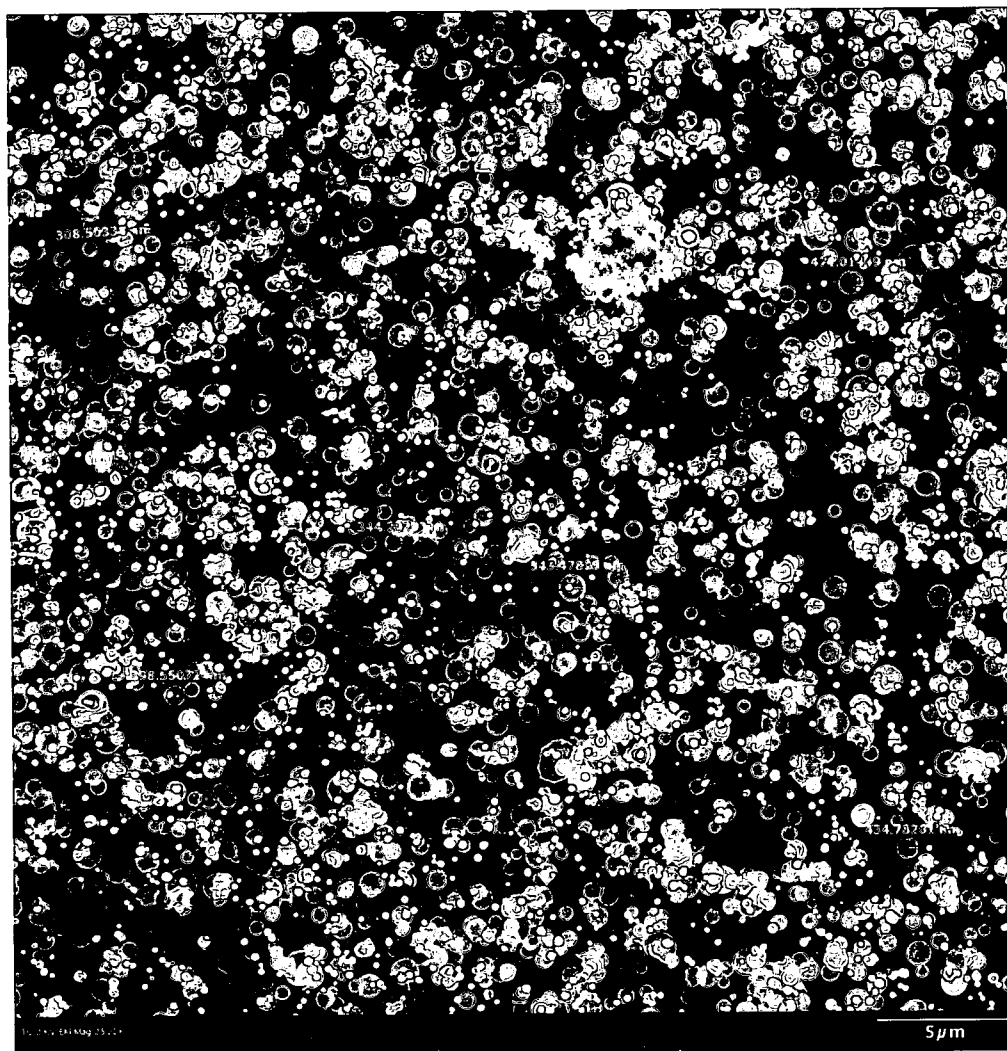


Figure 39 SEM micrograph of nanoparticles from experiment #5 at 2,500x magnification

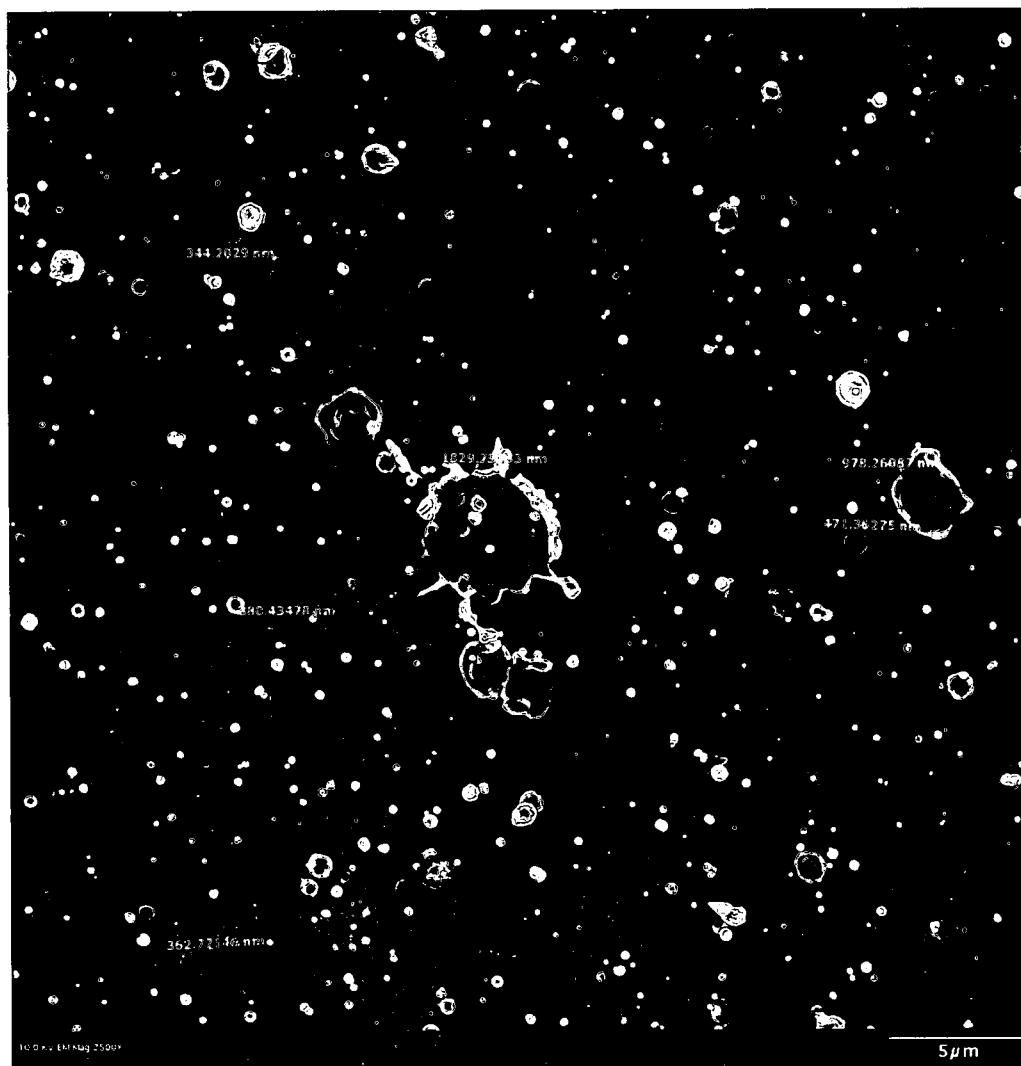


Figure 40 SEM micrograph of nanoparticles from experiment #6 at 2,500x magnification

Experiment #7 was performed without the ablation laser, no catalyst material was used. The CO₂ heating laser was used to illuminate floating CNTs. The results from this experiment are quite interesting. TEM micrographs from this experiment, located in Figures 41 and 42, show amorphous carbon covering the nanotubes. These micrographs were intentionally captured in an over-focused state in order to show the CNT walls inside the amorphous carbon. Figure 43 reveals a multiwall carbon nanotube protruding from a large mass of amorphous carbon. Additionally, other nanotubes can be seen inside the mass itself. This suggests that the Infrared (IR) absorption of solid carbon and ethylene gas contribute to growth.

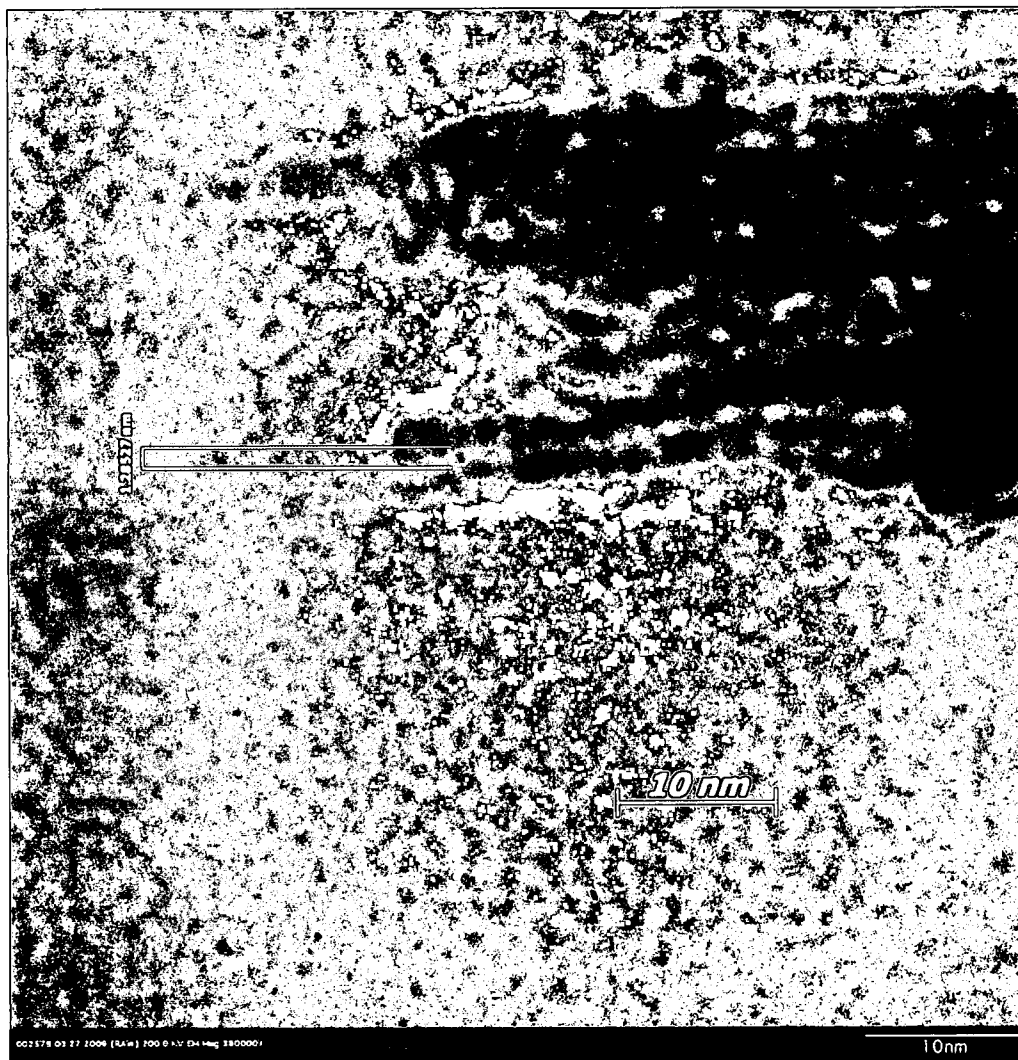


Figure 41 TEM micrograph from experiment #7 showing a 1.2 nm diameter CNT



Figure 42 TEM micrograph from experiment #7 showing a 3.7 nm diameter CNT

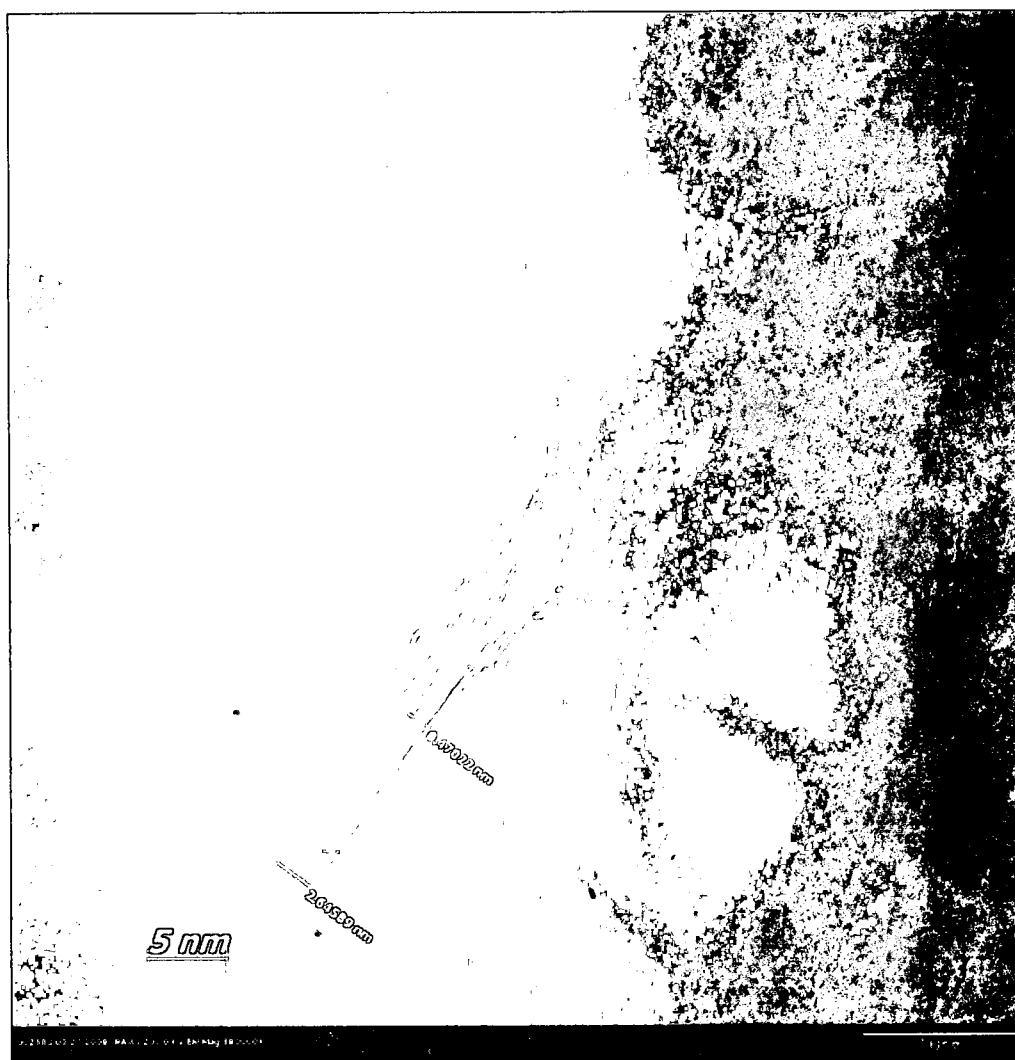


Figure 43 TEM micrograph from experiment #7 showing a 2.6 nm diameter MWCNT

Experiment #8 was conducted at 9.6 Torr to evaluate the effects of higher pressure. While higher pressure may have been more effective for CNT growth it appeared to be too high for generating the proper size nanoparticles with the TTFA process. Very few particles were found on the TEM grids and no nanotubes were observed.

Through the knowledge gained from previous experiments, experiment #9 was conducted at the lowest attainable pressure with similar mass flow rates. This was done in order to generate the best catalyst nanoparticles and had the side benefit of reducing the activity of the hydrocarbon gas. TEM micrographs were captured on an FEI Titan TEM. They appeared to have more nanotubes per unit area, but this is speculation because the entire grid was not able to be evaluated. Unfortunately, there were no free standing CNTs. Only CNTs coated with amorphous carbon, protruding from large masses carbonaceous masses. Figure 44 shows an amorphous carbon coated CNT protruding from a larger carbon mass. Figure 45 is an over-focused TEM micrograph of an area with many tube-like features. Figure 46 is an area from Figure 45 at a higher magnification that shows interesting wall-like features.

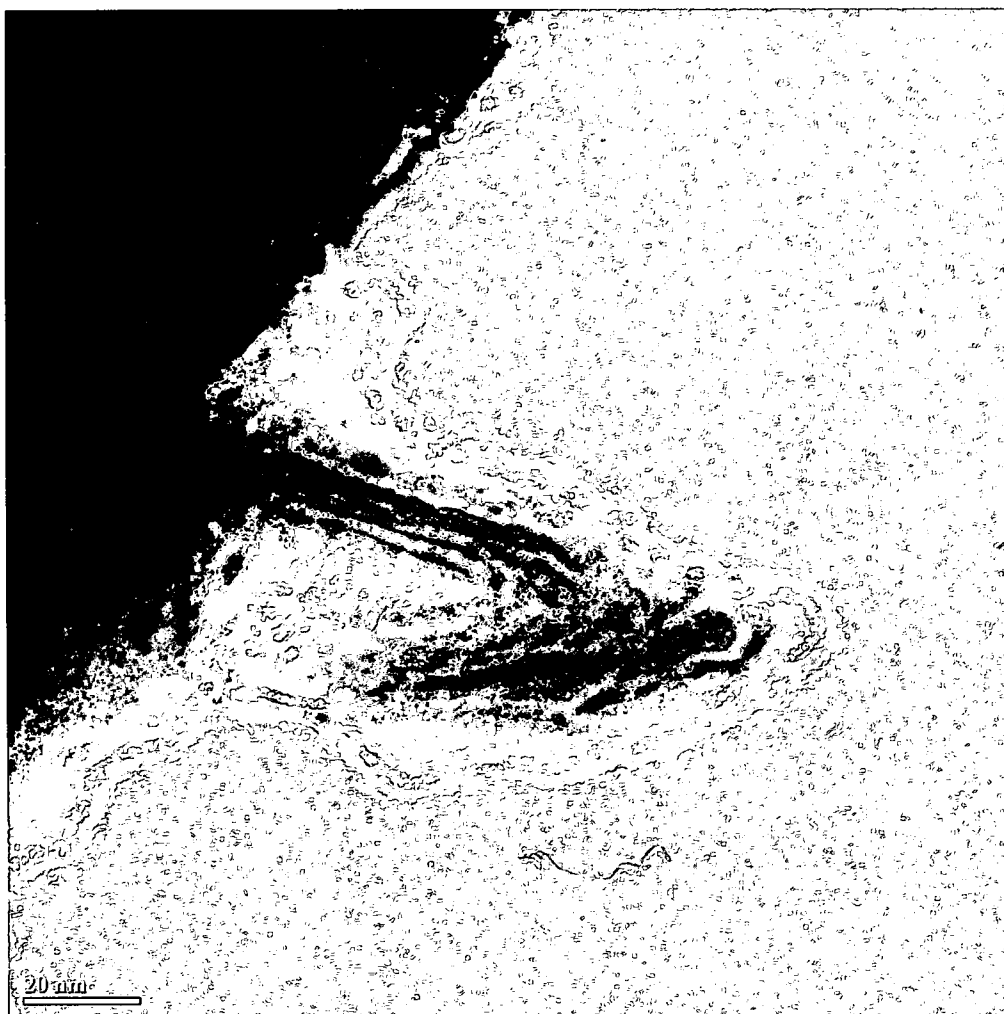


Figure 44 TEM micrograph of a CNT protruding from a larger carbon mass



Figure 45 An intentionally over-focused TEM micrograph showing many tube-like features



Figure 46 TEM micrograph of interesting wall-like features (circled)

3.2 Discussion

The growth observed from these experiments seems to be from a two-step process. First CNTs grow in catalytic nature and then a pyrolytic carbon deposition occurs [67]. The pyrolytic carbon deposition requires no catalyst and most likely occurs due to the heating of the ethylene. When one evaluates the infrared spectrum of ethylene in Figure 47 which was taken at 600 Torr with Path Length of 5 cm from the NIST Webbook [68], it can be seen that absorption is quite high from 950 nm to 11.5 μm . A close up of this region shown in Figure 48 reveals a particularly high absorption peak located at 10.55 μm . These peaks are a result of photon energy being absorbed and converted to vibrational and rotational energy. When a molecule is promoted to an excited state, the reaction rate may be increased due to the higher probability of collisions with neighboring atoms and molecules. Absorption can only occur when spacing between energy levels equals the photon energy. Stimulated absorption takes place from the zero-point energy until a mismatch occurs from the convergence of increasing energy levels according to the Morse Potential Energy Model. When incident photon energies no longer match the energy level spacing, absorption is forbidden. Additionally, photon emission can occur once the ionization energy is reached. This reduces the vibrational energy finite number of levels equivalent to the photon energy emitted.

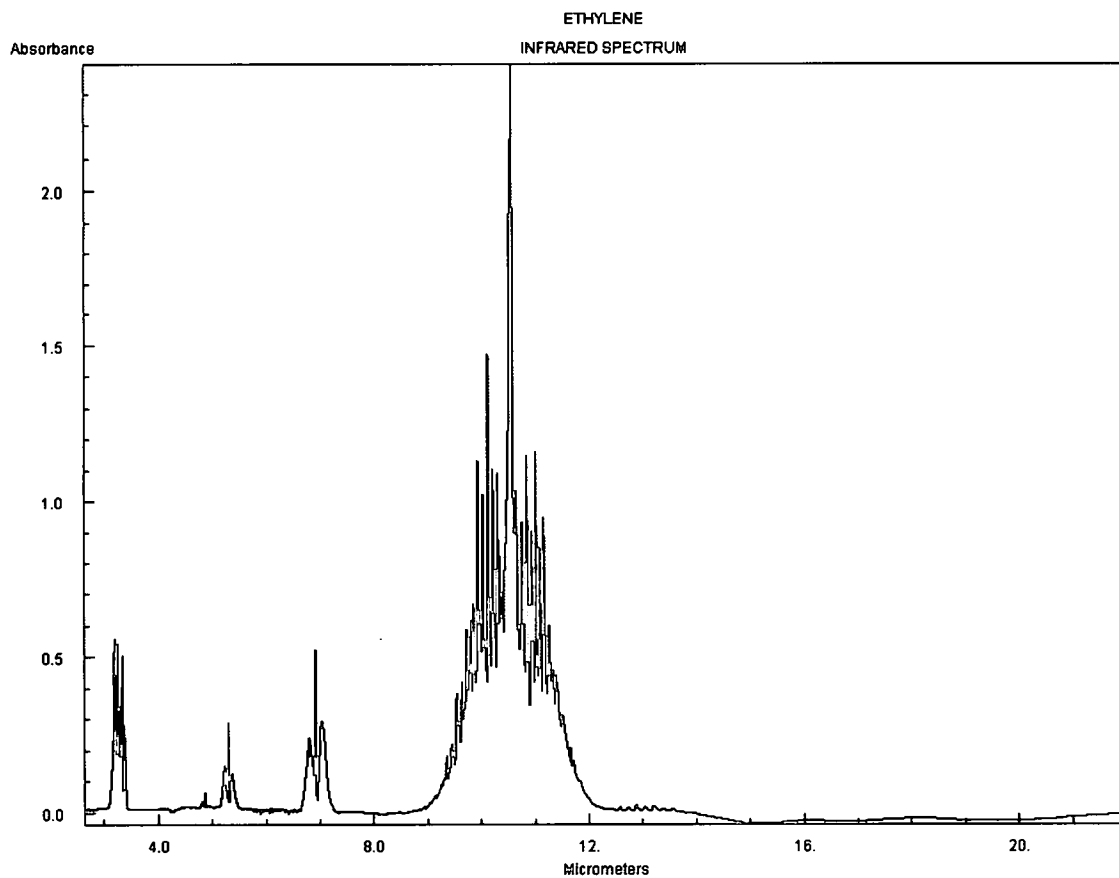


Figure 47 Infrared spectrum of ethylene at 600 Torr with path length of 5 cm from the NIST Webbook [66]

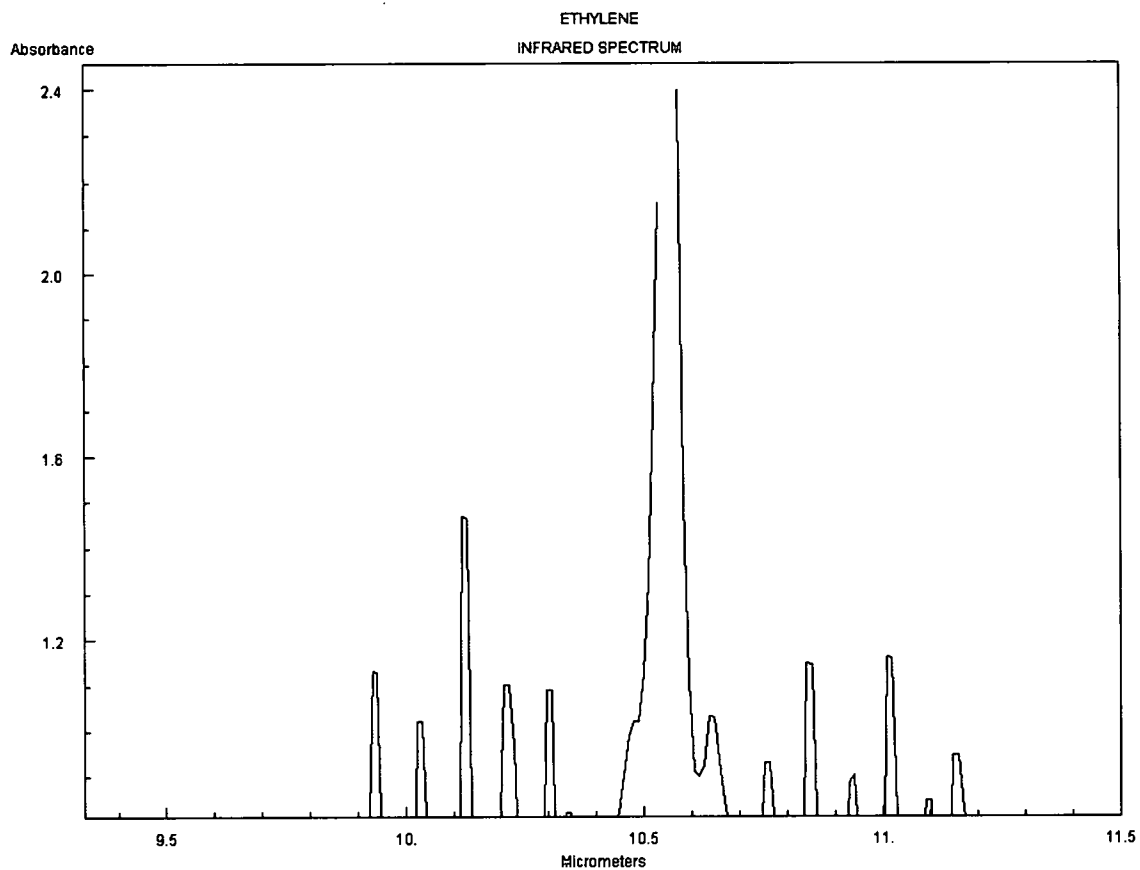


Figure 48 Close up of 9.0 – 11.5 μm region of ethylene IR spectrum from the NIST Webbook [66]

Chapter 4

Summary and Future Work

4.1 Summary

The TTFA method was successful for generating floating catalyst and producing CNTs. While the products were not pristine, an understanding of the mechanism CO_2 laser heating was developed. We believe that absorption of IR energy by solid carbon and the promotion of ethylene to excited vibrational levels contributed to the rapid growth of CNTs and amorphous carbon.

4.2 Future Work

While the CNT yields using TTFA and CO_2 heating laser appear to be small, the conditions may be optimized to increase these yields greatly. An ideal system would have a larger heating laser, capable of heating a spot size equal to the inside diameter of the extension tube. This would ensure that every particle traveling through the system would be heated equally. A mass flow controller with a dynamic range of 0-50 SCCM would be superior for optimizing the ethylene concentration within the chamber. The currently employed controller lacks the resolution to reliably operate at less than 25 SCCM. A reduced hydrocarbon concentration would likely reduce the excessive amounts of amorphous carbon that have been found to be coating CNTs in the products. An additional mass flow controller to insert a small amount of oxygen to etch away amorphous carbon would be beneficial as well.

Appendix

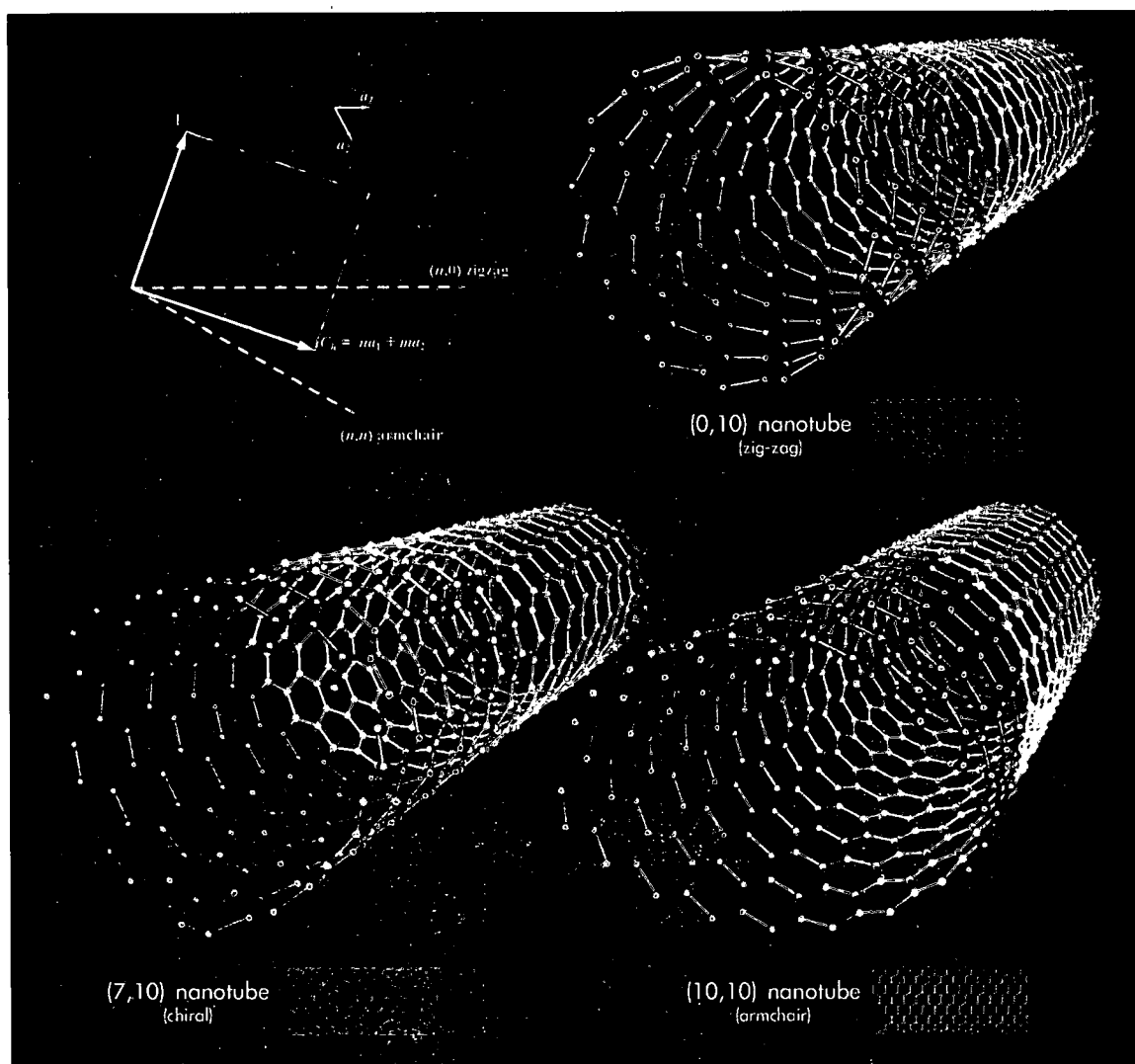


Figure 49 Illustration of three different SWNT chiralities [69]

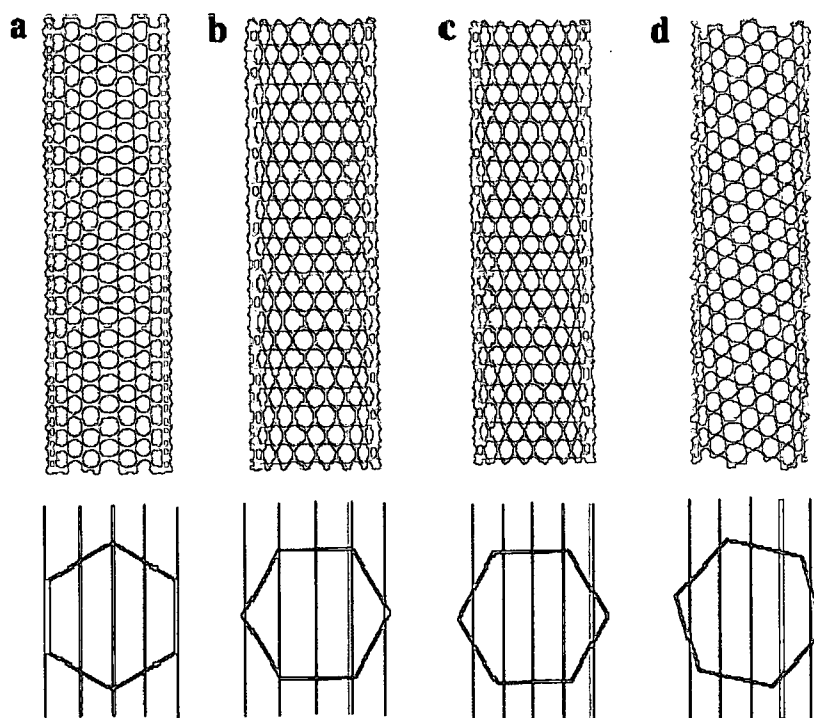


Fig. 3. Schematic structures of SWNTs and how they determine the electronic properties of the nanotubes. (a) A $(10,10)$ arm-chair nanotube. Bottom panel: the hexagon represents the first Brillouin zone of a graphene sheet in reciprocal space. The vertical lines represent the electronic states of the nanotube. The center-line crosses two corners of the hexagon, resulting in a metallic nanotube. (b) A $(12,0)$ zigzag nanotube. The electronic states cross the hexagon corners, but a small band gap can develop due to the curvature of the nanotube. (c) The $(14,0)$ zigzag tube is semiconducting because the states on the vertical lines miss the corner points of the hexagon. (d) A $(7,16)$ tube is semiconducting. This figure illustrates the extreme sensitivity of nanotube electronic structures to the diameter and chirality of nanotubes.

Figure 50 Diagram from H. Dai showing different SWNT structures with description of corresponding electronic properties [50]

REFERENCES

- 1 Kroto, H.W., Heath, J.R., O'Brien, S.C., Curl, R.F. Smalley, R.E., 1985, C60: buckminsterfullerene, *Nature* (London, UK), 318: 162-163.
- 2 Ebbesen, T.W., Ajayan, P.M., 1992, Large-scale synthesis of carbon nanotubes, *Nature* (London) 358: 220.
- 3 Seraphin, S., Zhou, D., Jaio, J., Withers, J.C., Loufty, R. 1993, Effect of processing conditions on the morphology and yield of carbon nanotubes, *Carbon*, 31: 685-689.
- 4 Iijima, S., 1991, Helical Microtubules of Graphitic Carbon, *Nature* 354: 56-58.
- 5 Iijima, S., Ichihashi, T., 1993, Single-shell carbon nanotubes of 1-nm diameter, *Nature* 363: 603-605.
- 6 Monthieux, M., Kuznetsov, V.L., 2006, Who should be given the credit for the discovery of carbon nanotubes?, *Carbon*, 44: 1621-1623.
- 7 Dresselhaus, M.S., Dresselhaus, G., Avouris, P., 2001, Carbon Nanotubes: Synthesis, Structure, Properties, and Applications, Springer, Berlin, 1-9.
- 8 Kingston, C.T., Zygmunt, J.J., Denommee, S., Simard, B., 2003, Efficient Laser Synthesis of Single-Walled Carbon Nanotubes Through Laser Heating of the Condensing Vaporization Plume, *Carbon* 42: 1657-1664.
- 9 Krupke, R., Hennrich, F., Löhneysen, H.V., Kappes, M.M., 2003, Separation of Metallic from Semiconducting Single-Walled Carbon Nanotubes, 301; 5631: 344-347.
- 10 Cheap Tubes Inc., Updated 31 March 2009, <http://www.cheaptubes.com/carbon-nanotubes-prices.htm>.
Ref Type: Electronic Citation
- 11 Saito, R., Dresselhaus, G., Dresselhaus, M.S., 1998, Physical Properties of Carbon Nanotubes, Imperial College Press, Covent Garden, London: 35.
- 12 Qin, L.C. Zhao, X., Hirahara, K., Miyamoto, Y., Ando, Y., Iijima, S., 2000, The smallest Carbon Nanotube, *Nature*, 408: 50.
- 13 Treacy, M.M.J., Ebbesen, T.W., Gibson, J.M., 1996, Exceptionally high Young's modulus observed for individual carbon nanotubes, *Nature*, 381: 678.

-
- 14 Meo, M., Rossi, M., 2006, Prediction of Young's modulus of single wall carbon nanotubes by molecular-mechanics based finite element modeling, *Composites Science and Technology*, 66: 1597-1605.
- 15 Saito, R., Dresselhaus, G., Dresselhaus, M.S., 1998, Physical Properties of Carbon Nanotubes, Imperial College Press, Covent Garden, London: 157.
- 16 Yao, Z., Kane, C.L., Dekker, C., 2000, High-Field Electrical Transport in Single-Wall Carbon Nanotubes, *Phys. Rev. Lett.*, 84: 2941.
- 17 Avouris, P., 2000, Carbon Nanotubes and Their Physical Properties, Michigan State University.
Ref Type: Lecture Notes
- 18 Kolgatin, S. N., Lev, M. L., Peregud, B. P., Stepanov, A. M., Fedorova, T. A., Furman, A. S., Khachatur'yants, A. V., 1989, Destruction of copper wire by the passage of currents with densities above 10^7 A/cm², *Žurnal tehničkoj fiziki*, 59;9: 123-133.
- 19 Immunologie et Chimie Thérapeutique / Vectorisation, Retrieved 9 May 2009, Functionalised carbon nanotubes as therapeutic vectors,
http://www-ibmc.u-strasbg.fr/ict/vectorisation/nanotubes_eng.shtml
Ref Type: Electronic Citation
- 20 Alexander, M.D., 1 September 2006.
Ref Type: Personal Communication
- 21 Hafner, J.H., Bronikowski, M.J., Azamian, B.R., Nikolaev, P., Rinzler, A.G., Colbert, D.T., Smith, K.A., Smalley, R.E., 1998, Catalytic Growth of Single-Wall Carbon Nanotubes from Metal Particles, *Chem. Phys. Lett.*, 296: 195-202.
- 22 Saito, R., Dresselhaus, G., Dresselhaus, M.S., 1998, Physical Properties of Carbon Nanotubes, Imperial College Press, Covent Garden, London: 349-351.
- 23 Tans, S.J., Devoret, M.H., Dai, H., Thess, A., Smalley, R.E., Geerligs, L.J., Dekker, C., 1997, Individual Single-Wall Carbon Nanotubes as Quantum Wires, *Nature*, 386:474-477.
- 24 Saito, R., Dresselhaus, G., Dresselhaus, M.S., 1998, Physical Properties of Carbon Nanotubes, Imperial College Press, Covent Garden, London: 379-380.
- 25 Applied Sciences Inc., Retrieved 26 March 2009, Pyrograf® Products Incorporated: Pyrograf III, <http://www.apsci.com/ppi-pyro3.html>
Ref Type: Electronic Citation

-
- 26 Endo Laboratory, Updated 29 July 2005, Retrieved 13 March 2009, Applications for the composite material of carbon fiber,
<http://endomoribu.shinshu-u.ac.jp/research/cnt/composit.html>
Ref Type: Electronic Citation
- 27 Frank, S., Poncharal, P., Wang, Z.L., Heer, W.A., 1998, Carbon Nanotube Quantum Resistors, *Science*, 280;5370: 1744-1746.
- 28 Dillon, A. C., Jones, K. M., Bekedahl, T. A., Kang, C. H., Bethune, D. S., Heben, M. J., 1997, Storage of Hydrogen in Single-Walled Carbon Nanotubes, *Nature*, 386: 377.
- 29 Bellucci, S., 2005, Carbon Nanotubes: Physics and Applications, *phys. stat. sol.* 2, 1: 34-47.
- 30 Robertson, J., 2004, Realistic application of CNTs. *Mater Today*, 7(10):46-52.
- 31 Yakobson B.T., Smalley, R.E., 1997, Elastic buckling of single-walled carbon nanotube ropes under high pressure, *Am. Sci.* 85: 324.
- 32 Berber, S., Kwon, Y., Tománek, D., 2000, Unusually High Thermal Conductivity of Carbon Nanotubes, *Phys. Rev. Lett.*, 84:4613-4616.
- 33 Saito, S., 1997, Carbon Nanotubes for Next-Generation Electronics Devices, *Science*, 278: 77.
- 34 Martel, R., Schmidt, T., Shea, H.R., Hertel, T., Avouris, Ph., 1998, Single- and multi-wall carbon nanotube field-effect transistors, *Appl. Phys. Lett.*, 73: 2447.
- 35 Niu, C., Sichel, E.K., Hoch, R., Moy, D., Tennent, H., 1997, High power electrochemical capacitors based on carbon nanotube electrodes, *Appl. Phys. Lett.*, 70: 1480.
- 36 Wang, Q.H., Setlur, A.A., Lauerhaas, J.M., Dai, J.Y., E. W. Seelig, E.W., Chang R.P.H., 1998, A nanotube-based field emission flat panel display, *Appl. Phys. Lett.* 72: 2912-2913.
- 37 Kim, H.M., Kim, K., Lee, C.Y., Joo, J., Cho, S.J., Yoon, H.S., Pejakovic, D.A., Yoo, J.W., Epstein, A.J., 2004, Electrical conductivity and electromagnetic interference shielding of multiwalled carbon nanotube composites containing Fe catalyst, *Appl. Phys. Lett.*, 84: 589.
- 38 Hockanson, D.M., Zhang, R., Zacharisen, G., Malladi, D., Issued 13 September 2003, EMI shielding apparatus, US Patent 6944025.

-
- 39 Colbert, D.T., 2003, Single-wall nanotubes: a new option for conductive plastics and engineering polymers, *Plastics Additives & Compounding*, 391:1464.
- 40 Ramasubramaniam, R., Chen, J., Liu, H., 2003, Homogeneous carbon nanotube/polymer composites for electrical applications, *Appl. Phys. Lett.*, 83: 2928.
- 41 Black B.M., Alexander M.D., Dowty H.J., 2007, Spray Methods for Improved Shielding Effectiveness of Conductive Nanofiber Composites (ITAR), *SAMPE Journal*, 44(2), 141.
- 42 Lide, D.R., 1994, *CRC Handbook of Chemistry and Physics 75th ed.* Boca Raton, CRC Press: 12-41.
- 43 Dresselhaus, M.S., Dresselhaus, G., Avouris, P., 2001, Carbon Nanotubes: Synthesis, Structure, Properties, and Applications, Springer, Berlin, 11.
- 44 Air Canada, Retrieved 29 March 2009, Aircanada.com - About Air Canada - Historical Fleet, <http://www.aircanada.com/en/about/fleet/historical/b747-400.html>
Ref Type: Electronic Citation
- 45 Iijima, S., Brabec, C., Maiti, A., Bernhole, J., 1996, Structural flexibility of carbon nanotubes, *J. Chem. Phys.*, 104: 2089-2092.
- 46 Zhang, M., Atkinson, K.R., Baughman, R.H., 2004, Multifunctional Carbon Nanotube Yans by Downsizing Ancient Technology, *Science*, 306; 5700: 1358-1361.
- 47 Thostenson, E.T., Ren, Z., Chou, T.W., 2001, Advances in the Science and Technology of Carbon Nanotubes and Their Composites: a Review, *Composites Science and Technology*, 61;13: 1899-1912.
- 48 Atkins, P.W., DePaula, J., 2002, *Physical Chemistry – 7th ed.*, W.H Freeman and Company, New York: 750-751.
- 49 Journet, C., Maser, W.K. Bernier P., Loiseau, A., Lamyde L.C., Lefrant, S., Deniard, P., Leek, R., Fischerk, J.E., 1997, Large-scale production of single-walled carbon nanotubes by the electric-arc technique, *Nature*, 388: 756-758.
- 50 Dai, H., Rinzler, A. D., Nikolaev, P., Thess, A., Colbert, D. T., Smalley, R. E., 1996, Single-wall nanotubes produced by metal-catalyzed disproportionation of carbon monoxide, *Chem. Phys. Lett*, 260, 471-475.
- 51 Saito Y., K. , Hamaguchi, K., Hata, K., Tohji, A., Kasuya, Y., Nishina, K., Uchida, Y., Tasaka, F., Ikazaki, Yumura, M.. 1998, Field Emission from Carbon Nanotubes; Purified Single-Walled and Multi-Walled Tubes, *Ultra microscopy*, 73: 1.

52 Kong, J., Cassell, A.M., Dai, H., 1999, Chemical vapor deposition of methane for single-walled carbon nanotubes, *Chem. Phys. Lett.*, 292; 4-6: 567-574.

53 Nikolaev, P., Bronikowski, M.J., Bradley, R.K., Rohmund, F., Colbert, D.T., Smith, K.A., Smalley, R.E., 1999, Gas-Phase Catalytic Growth of Single-Walled Carbon Nanotubes from Carbon Monoxide, *Chem. Phys. Lett.*: 91-97.

54 Murray, P.T., 14 March 2009, Carbon Nanotubes, MAT 604 - Nanostructured Materials.

Ref Type: Lecture Notes

55 Guo, T., Nikolaev, P., Thess, A., Colbert, D.T., Smalley, R.E., 1995, Catalytic growth of single-walled nanotubes by laser vaporization, *Chem. Phys. Lett.*, 243: 49-54.

56 Thess, A., Lee, R., Nikolaev, P., Dai, H., Petit, P., Robert, J., Xu, C., Lee, Y.H., Kim, S.G., Rinzler, A.G., Colbert, D.T., Scseria, G.E., Tomanek, D., Fischer, J.E., Smalley, R.E., 1996, Crystalline ropes of metallic carbon nanotubes, *Science*, 273: 483-487.

57 R ummeli, M.H., Kramberger, C., L offler, M., Jost, O., Bystrzejewski, M., Gruneis, A., Gemming, T., Pompe, W., Buchner, B., Pichler, T., 2007, Catalyst Volume to Surface Area Constraints for Nucleating Carbon Nanotubes, *J. Phys. Chem. B*, 111: 8234,8241.

58 Ready, J.F., 1963, Development of Plume of Material Vaporized by Giant-Pulse Laser, *Applied Physics Letters*, 3:11.

59 Willmott, P.R., Huber, J.R., 2000, Pulsed laser vaporization and deposition, *Reviews of Modern Physics*, 72:315.

60 Back, T., 2 October 2008

Ref Type: Private Communication

61 Murray, P.T., Shin, E., 2008, Formation of silver nanoparticles by through thin film ablation, *Materials Letters*, 62, 4336-4338.

62 R ummeli, M.H., Kramberger, C., Sch ffel, F., Borowiak-Palen E., Gemming, T., Rellinghaus, B., Jost, O., L offler, M., Ayala, P., Pichler, J. Kalenczuk, T., R. 2007, Catalyst Size Dependencies for Carbon Nanotube Synthesis, *Physica Status Solidi*, 244, No. 11: 3911-3915.

63 Huang, S., Cai, X., Liu, J. 2003 Growth of Millimeter-Long and Horizontally Aligned Single-Walled Carbon Nanotubes on Flat Substrates, *JACS*, 125:19, 5637.

64 Synrad, 2006, Series L48 Lasers Operator's Manual, SYNRAD, Inc. 4600 Campus Place Mukilteo, WA: 3-4.

65 Bazhenov, A.V., Kveder, V.V., Maksimov, A.A., Tartakovskii, I.I., Oganyan, R.A., Ossipyan, Yu.A., Shalynin, A.I., 1998, Raman Scattering of Light and IR Absorption in Carbon Nanotubes, *J. Exper. Theor. Phys.*, 86,5: 1030-1034.

66 Bachilo, S.M., Strano, M.S., Kittrell, C., Hague, R.H., Smalley, R.E., Carbon Nanotubes, *Science*, 298: 2361-6.

67 Endo, M., Takeuchi, K., Kobori, K., Takahashi, K., Kroto, H.W., Sarkar A., 1995, Pyrolytic carbon nanotubes from vapor-grown carbon fibers, *Carbon*, 33:873-81.

68 NIST webbook, 2009, Ethylene Infrared Spectrum, Retrieved 7 January 2009
<http://webbook.nist.gov/cgi/cbook.cgi?ID=C74851&Units=SI&Mask=80#IR-Spec>.
Ref Type: Electronic Citation

69 Ströck, M., Updated: 1 February 2006, A diagram showing the types of carbon nanotubes, http://en.wikipedia.org/wiki/File:Types_of_Carbon_Nanotubes.png
Ref Type: Electronic Citation

2062594307